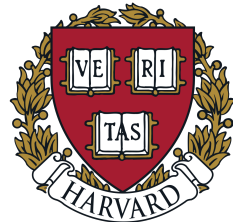


Cluster Analysis of N₂O Enhancements Observed by ATom

A Thesis Presented
by
Ethan Manninen
to
the Department of Earth and Planetary Sciences
in partial fulfillment of the requirements
for a degree with honors of Bachelor of Arts

April 2021

Harvard College



Abstract

In this work, we address the following questions: 1) What is the balance between global transport and regional emissions in the vertical structure of N₂O mixing ratios in the African outflow? 2) Is it possible to distinguish different combustion sources of N₂O in Africa? 3) Can we confirm or deny the possibility of a heterogeneous chemical N₂O source in air heavily polluted by urban-industrial emissions? 4) How do N₂O enhancements modeled from ATom observations compare to current understanding of N₂O budgets in the region? 5) What is the total amount of N₂O flowing through the African outflow? N₂O is the third most important greenhouse gas and the most important ozone depleting gas; understanding these contributions to its African regional budget is an important piece of the climate puzzle. We analyze trace gas data gathered by the Atmospheric Tomography Mission, with a focus on N₂O in the Atlantic basin. We use a clustering technique built around the DBSCAN and t-SNE algorithms to improve understanding of different N₂O sources. Some Atlantic ATom clusters are broadly characterizable as part of the African outflow. N₂O enhancements in the ATom 2 African outflow are associated with combustion emissions. Within these emissions, we find an enhancement from anthropogenic biomass burning, a possible enhancement from heterogeneous chemistry, and an important transport contribution from Europe. The urban biomass burning source we identified is associated with discrepancies between ATom N₂O modeled enhancements and a recent landmark N₂O budget. We evaluate N₂O enhancements outside of the African outflow and find that aged pollution is an important driver of N₂O. We also develop a technique to estimate the atmospheric N₂O background using atmospheric transport models and global ATom N₂O data. This method also shows that advection is a crucial process in the arrangement of N₂O in the African outflow. We use this more region specific model of N₂O enhancements to find 0.9-1.1 Tg N yr⁻¹ of N₂O flowing through the African outflow. We also use a more global N₂O background to find 1.9-2.1 Tg N yr⁻¹ of N₂O flowing through the African outflow. Emissions from burning wood and urban-industrial emissions with high sulfur content, along with transport processes, are the key to our understanding of N₂O in the African outflow.

Contents

Acknowledgements	v
1 Introduction	1
1.1 Why do we care about N ₂ O?	1
1.2 N ₂ O Budget and Trend	2
1.3 N ₂ O Source and Sink Processes	3
1.3.1 Non-Combustion Sources	3
1.3.2 Combustion Sources	3
1.3.3 Stratospheric Sink	7
1.4 More Motivation	7
2 Methods	9
2.1 The Atmospheric Tomography Mission	9
2.2 Calculation of Footprints to Assess Surface Influence	10
2.2.1 Overview of the Stochastic Time-Inverted Lagrangian Transport Model	11
2.2.2 TRAJ3D Trajectories	12
2.2.3 STILT to Calculate Footprints from TRAJ3D Trajectories	13
2.3 Clustering	17
2.4 Repeated Multiple Linear Regression with Bayesian Information Criterion for Model Selection and Analysis	19
2.5 Enhancement and Flux Calculation	21
2.5.1 Modeling the Atmospheric Background of N ₂ O, CO, and CH ₄	21

2.5.2	Flux Calculation	27
2.6	Convolving Emissions Fields to Compare with ATom Values	28
2.7	Statistics, Math, and Code	29
3	Results and Discussion	30
3.1	Combustion Sources of N ₂ O and the African Outflow	30
3.1.1	Interhemispheric Transport of N ₂ O	34
3.1.2	Possible Heterogeneous Chemical Source of N ₂ O	36
3.2	Analysis of Non-African Outflow N ₂ O Enhancements	37
3.3	Comparison with <i>Tian et al. (2020)</i>	40
3.4	Quantifying Flux	43
4	Conclusion	46
A	Appendix	50
References		70

List of Figures

1.1	<i>Wang et al. (2020)</i> Heterogeneous N ₂ O Formation Redox Reaction	5
1.2	<i>Wang et al. (2020)</i> Heterogeneous N ₂ O Formation Observed Mixing Ratios	6
2.1	Flight Paths of Atlantic Atom	10
2.2	STILT Schematic	16
2.3	Clustering Methodology Schematic	18
2.4	Interpolated N ₂ O, CO, CH ₄ Mixing Ratio Curtains	23
2.5	Evaluation of Back Trajectories for Modeling the Background Mixing Ratio of Trace Gasses	24
2.6	Profiles of Two Background Models and Observed Mixing Ratios of N ₂ O, CO, CH ₄	26
3.1	ATom 2 N ₂ O and Biomass Burning Tracers	31
3.2	Cluster Analysis of Combustion Emitted N ₂ O	32
3.3	MODIS Fire Data	33
3.4	Interhemispheric Transport of N ₂ O	34
3.5	Correlations Between Species Associated with Heterogeneous N ₂ O Formation Pathways	37
3.6	Non-African Outflow Repeated Multiple Linear Regression Analysis	39
3.7	<i>Tian et al. (2020)</i> vs ATom Estimate of Interhemispheric N ₂ O Transport	41

3.8 Comparison of ATom Observed N ₂ O Enhancement with <i>Tian et al.</i> (2020)	42
3.9 Repeated Multiple Regression Analysis of ATom vs. <i>Tian et al.</i> (2020) N ₂ O Enhancement Residuals	43
3.10 Integrated Trace Gas Fluxes in the African Outflow	45
A.1 Zonal Wind in the African Outflow	50
A.2 Profiles of Modeled Background N ₂ O on Feb. 13 2017	51
A.3 Profiles of Modeled Background N ₂ O on Feb. 15 2017	52
A.4 Profiles of Modeled Background CO on Feb. 13 2017	53
A.5 Profiles of Modeled Background CO on Feb. 15 2017	54
A.6 Profiles of Modeled Background CH ₄ on Feb. 13 2017	55
A.7 Profiles of Modeled Background CH ₄ on Feb. 15 2017	56
A.8 Transect of N ₂ O Enhancement over Modeled Backgrounds . .	57
A.9 Transect of N ₂ O Flux from Modeled Backgrounds	57
A.10 Average Footprints of ATom 2 Clusters	58
A.11 Average Footprints of ATom 3 Clusters	59
A.12 Average Footprints of ATom 4 Clusters	60
A.13 Profile of ATom 2 Clusters	61
A.14 Profile of ATom 4 Clusters	61

This thesis only has my name on the title page, but it would not exist without the following people:

Steven Wofsy, with inexhaustible patience and wisdom, worked countless hours to evolve me from a person who simply likes math and atmospheric chemistry into a researcher.

The rest of Team N₂O—Yenny Gonzalez-Ramos, Róisín Commane, and Luke Schiferl —gave me their kindness and clever ideas, and helped with calculations.

The Earth and Planetary Science Preceptors —Annika Quick and Esther James —taught me the nuts and bolts of a long-term research project and did their best to keep me on a timeline.

My family have done everything and anything for me my entire life.

Rachel Oshiro was unconditionally there for me, no matter what thesis induced mood I could come up with. She also helped with Adobe Illustrator.

The Harvard University Center for the Environment and Harvard Earth and Planetary Sciences Department funded my work over the summer of 2019, and the Wofsy-Munger Group on Biosphere-Atmosphere Exchange funded my work over the summer of 2020.

Chapter 1

Introduction

1.1 Why do we care about N₂O?

Humanity's impact on the trace gas composition of the atmosphere increases with the population and complexity of our global civilization. This is of great concern primarily due to the effects anthropogenically forced gasses—including carbon dioxide (CO₂), methane (CH₄), nitrous oxide (N₂O) and chloroflourocabons (CFC's)—have on the radiative properties of the atmosphere. Nitrous oxide is the third most important greenhouse gas (*Caias et al.*, 2013). It lasts longer in the atmosphere than CH₄ and causes more warming per molecule than CO₂ (*Butterbach-Bahl et al.*, 2013; *Prather et al.*, 2015). Some trace gasses, notably CFC's, are also of interest because they strengthen the chemical sinks of stratospheric ozone, which protects the surface from high energy solar radiation (*Molina and Rowland*, 1974; *Anderson et al.*, 1991). With CFC concentrations decreasing in the atmosphere as a result of the Montreal Protocol, N₂O catalyzes the primary chemical sink for stratospheric ozone (*Ravishankara et al.*, 2009). We study N₂O as a potential threat to the ozone layer and to better understand human driven climate change.

The goal of this project is to use data gathered by the Atmospheric Tomography Mission (ATom) to advance our understanding of atmospheric N₂O, especially enhancements observed in the African outflow. Specifically,

we seek to isolate enhancements from different combustion processes, understand the relevance of advective transport, and investigate the possibility of a source of N₂O from heterogeneous chemistry. We also are interested in how ATom observations of N₂O differ from models of N₂O in the literature, and what processes are associated with those differences. Finally, we want to model the total amount of N₂O emitted by Africa to the outflow.

1.2 N₂O Budget and Trend

Recent work by *Tian et al.* (2020) distilled modern understanding of global N₂O budgets. They found that 17 Tg N worth of N₂O are emitted annually to the atmosphere from natural and anthropogenic sources. Anthropogenic sources account for 43% of the total N₂O source, representing a significant perturbation. Photolysis and reaction with excited atomic oxygen, O¹D, in the upper stratosphere are the only significant sinks for atmospheric N₂O (*Prather et al.*, 2015). These processes remove 13.5 Tg N worth of N₂O from the atmosphere every year.

The difference between N₂O emissions and sinks results in 4.1 Tg N of N₂O accumulating in the atmosphere each year (*Tian et al.*, 2020). Observed and modeled changes in N₂O mixing ratios are around +0.75 ppb yr⁻¹, and the background mixing ratio has increased more than 20% from a preindustrial mixing ratio of 270 ppb to more than 330 ppb today (*Meure et al.*, 2006; *Yang et al.*, 2020; *Tian et al.*, 2020). The yearly change in N₂O concentrations is increasing more rapidly than accounted for in climate models, giving urgency to the problem of understanding the complex sources of N₂O (*Thompson et al.*, 2019).

1.3 N₂O Source and Sink Processes

1.3.1 Non-Combustion Sources

Soil microbes performing nitrification and denitrification are the single largest source of N₂O emissions (*Tian et al.*, 2019). 60-80% of the anthropogenic source of N₂O is from fertilizer production and application, which stimulates these nitrogen processing soil microbes to release more N₂O (*Galloway et al.*, 2003; *Gvakharia et al.*, 2020). Another important contributor to agricultural N₂O is livestock manure and excreta (*Dangal et al.*, 2019).

N₂O is produced primarily by denitrification, nitrification, and other more esoteric processes by ocean microbes in the water column (*Forster et al.*, 2009; *Santoro et al.*, 2011). The oceanic source is highly concentrated in upwelling regions, such as the Eastern Tropical Pacific, and the Benguela (*Nevison et al.*, 2004; *Yang et al.*, 2020). Humans perturb these processes by adding reactive nitrogen to the water column through fertilizer runoff (*Naqvi et al.*, 2000). In order to understand the impact of oceanic nitrogen cycle microbes on airborne N₂O observations, it is possible to use the product Atmospheric Potential Oxygen (APO). APO is calculated from oxygen to nitrogen ratios, and is a tracer of gas exchange between the atmosphere and ocean (*Stephens et al.*, 1998). However, it also can be influenced by biomass burning (*Lueker et al.*, 2003).

1.3.2 Combustion Sources

Various combustion processes release N₂O. Fossil fuel combustion reacts oxygen with both molecular nitrogen (N₂) in the air and nitrogen

in the fuel to make various forms of reactive nitrogen, including N₂O (*Gal- loway et al.*, 2003). Burning wood is another source of N₂O to the atmosphere (*Crutzen et al.*, 1979; *der Werf et al.*, 2010). Cities like Lagos, Nigeria, a large and rapidly growing city in Western Africa, generate N₂O by burning low quality petroleum products as well as wood for fuel (*Marais et al.*, 2014). Africa also has strong seasonal wildfires that produce a plume of pollution that extends into the Atlantic (*Schill et al.*, 2020).

Carbon monoxide (CO) is a useful tracer for combustion because of its short atmospheric lifetime (*Crutzen and Andreae*, 1990). Observing a CO enhancement indicates combustion influence, and observing an enhancement of another species (e.g. N₂O) in tandem with CO can indicate that species was emitted in the same location as the combustion. While CO is a tracer of general combustion, hydrogen cyanide (HCN) is specific to biomass burning, including natural forest fires and humans using wood or charcoal for fuel.

There is another potential source of N₂O related to combustion. Heterogeneous atmospheric chemistry is chemical processes that occur on the interface between gaseous species and aerosols. Current understanding does not account for a chemical source of N₂O in the atmosphere. Early work by *Martin et al.* (1981) found aqueous reaction pathways where nitrogen oxides (NO_x), and in particular nitrogen dioxide (NO₂), oxidize sulfur dioxide (SO₂) in solution, resulting in N₂O. They predicted this would not be a globally important source of N₂O to the atmosphere. *Pires and Rossi* (1997) and *Pires* (1996) investigated NO_x—SO₂ chemistry in lab simulated exhaust gas and found significant rates of heterogeneous N₂O production. All three of these studies find that the acidic environment created by the general oxidation of SO₂ to sulfuric acid is necessary to make N₂O.

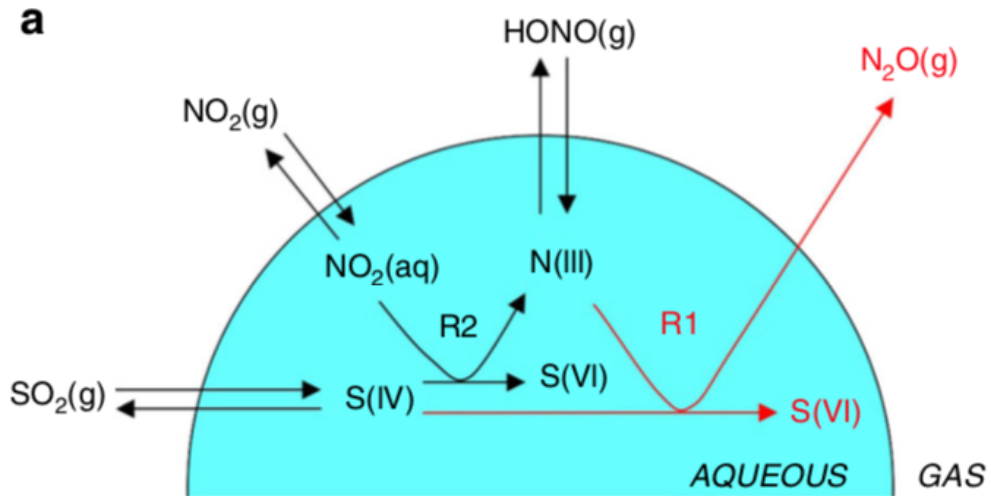


Figure 1.1: *Wang et al. (2020)*'s schematic of their proposed heterogeneous reaction pathway. SO₂ is oxidized to SO₄²⁻ in steps by NO_x and HONO in water droplets. The theoretical stoichiometry of this reaction would result in 1 mol of N₂O produced for every 3 mols SO₂ oxidized.

In their work investigating the Beijing winter haze phenomenon, *Wang et al. (2020)* found SO₂ oxidation by NO_x to be relevant to the production of sulfate particulate matter (PM). Their proposed pathway starts with gaseous NO₂ and SO₂, creates and uses nitrous acid (HONO) in an intermediary redox step, before adding aqueous sulfate to the aerosol particle and releasing N₂O (Figure 1.1). The theoretical stoichiometry of this pathway results in every 3 mols of SO₂ creating 1 mol of N₂O when oxidized. Observations of a Beijing haze event saw a roughly 5.5 ppb increase in N₂O alongside the 12 ppb increase in SO₂ (Figure 1.2). This reaction represents the possibility of a heterogeneous chemical N₂O source in concentrated, cloud processed urban pollution, and does not require the hot and acidic exhaust conditions of *Pires and Rossi (1997)*. They find evidence of this pathway under conditions with: high black carbon (BC), high liquid water content (condensed water droplets as opposed to just high relative humidity), as well as high NO_x and SO₂.

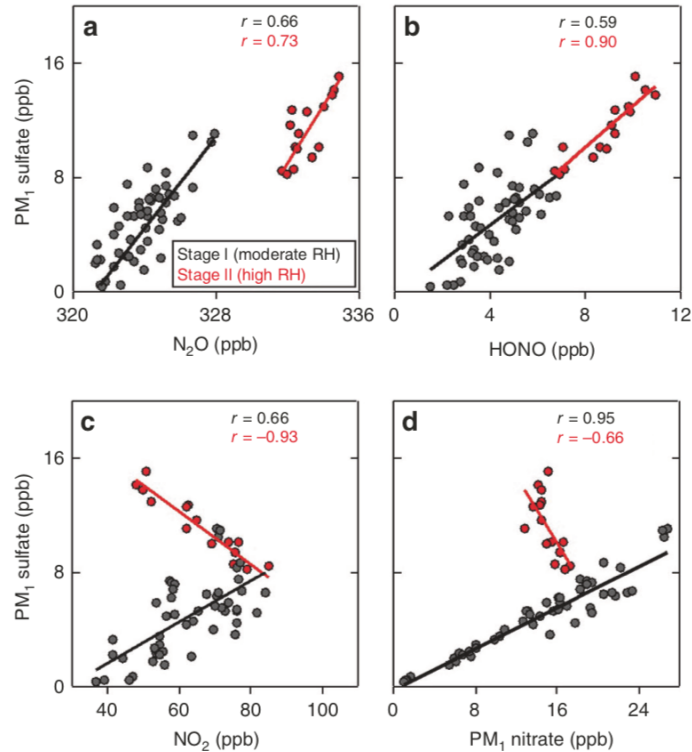


Figure 1.2: (Wang *et al.*, 2020)'s correlations between sulfate PM mixing ratios and **A**: N₂O, **B**: HONO **C**: NO₂, **D**: nitrate PM 1. They find that an increase of ≈ 12 ppb of sulfate PM corresponds to a ≈ 5.5 ppb increase in N₂O.

1.3.3 Stratospheric Sink

On average, N₂O lasts for 116 years in the atmosphere before being destroyed by photolysis or oxidation in the stratosphere (*Prather et al.*, 2015). As a result, the stratosphere is depleted in N₂O relative to the troposphere, leading to stratospheric-tropospheric exchange being modeled as the primary cause of the N₂O seasonal cycle (*Nevison et al.*, 2011). Work by *Gonzalez et al.* (2021) analyzed airborne observations of this phenomenon. They found that the effect of stratospheric-tropospheric exchange on Northern hemisphere surface N₂O mixing ratios lags by 2-3 months. The primacy of this process over emissions to the global N₂O background mixing ratio highlights the importance of transport to understanding airborne observations of N₂O.

1.4 More Motivation

As a final motivating exercise, we perform a back-of-the-envelope calculation comparing the climate impact represented by *Tian et al.* (2020)'s uncertainty for African N₂O emissions to the climate impact of operating a coal fired power plant. In *Tian et al.* (2020)'s regional analysis of N₂O flux, Africa had the greatest uncertainty. For the sake of argument, we assume the magnitude of that uncertainty is 1 Tg N worth of N₂O per year. Each molecule of N₂O has 298 times the 100 year global warming potential of a molecule of CO₂ (*Butterbach-Bahl et al.*, 2013). Assuming that the 1100 MW coal power plants newly built in Germany (*Wilkes and Parkin*, 2020) burn 10 Gg of coal per day equivalent to 3.65 Tg coal per year (*Donev et al.*, 2019), and assuming that coal is on average 70% carbon by weight (*U.S.EIA*, 2020), and assuming that all of the carbon in the burned coal eventually becomes

CO_2 in the atmosphere, we arrive at:

$$1\text{Tg N worth of N}_2\text{O} * \left(\frac{1 \text{ mol N}_2\text{O}}{28 * 10^{-12} \text{ Tg N worth of N}_2\text{O}} \right) * \left(\frac{298 \text{ mols CO}_2}{1 \text{ mol N}_2\text{O}} \right) * \\ \left(\frac{12 * 10^{-12} \text{ Tg carbon}}{1 \text{ mol CO}_2} \right) * \left(\frac{1 \text{ Tg coal}}{0.7 \text{ Tg carbon}} \right) * \left(\frac{1 \text{ coal powerplant}}{3.65 \text{ Tg coal}} \right) \approx \\ \boxed{50 \text{ coal powerplants!}}$$

(1.1)

Reducing uncertainty in African N_2O emissions is an important contribution to climate change research. Now sufficiently motivated, we set to work.

Chapter 2

Methods

2.1 The Atmospheric Tomography Mission

The Atmospheric Tomography Mission (ATom) was a series of four global flight campaigns that measured numerous chemical species with several instruments aboard the NASA DC-8 (*Wofsy et al.*, 2018). ATom flew in all four seasons between 2016-2018. Each campaign sampled the Atlantic and Pacific basins, as far from human activity as possible, as well as the Arctic and Antarctic, in profiles spanning roughly altitudes of 150 meters to 13,000 meters. The profiles of greatest interest to this study's consideration of African N₂O enhancements occurred on February 13 2017 and February 15 2017, (ATom 2).

The Quantum Cascade Laser Spectrometer (QCLS) was onboard the DC-8 to measure N₂O, CO, and CH₄ at 1 hz frequency. *Gonzalez et al.* (2021) analyzed the spectrographic data from the QCLS to give an N₂O mixing ratio. The QCLS was damaged for ATom 1 resulting in unusable N₂O data. Furthermore, in ATom 2, 3, and 4, QCLS had calibration issues due to sensitivity to the pressure and temperature in the cabin of DC-8 which resulted in drifts of the N₂O data. *Gonzalez et al.* (2021) used an algorithm based on principal component analysis to improve the accuracy of interpretation of raw QCLS data into N₂O mixing ratio measurements in spite of these drifts. They also validated their calculated N₂O values with the

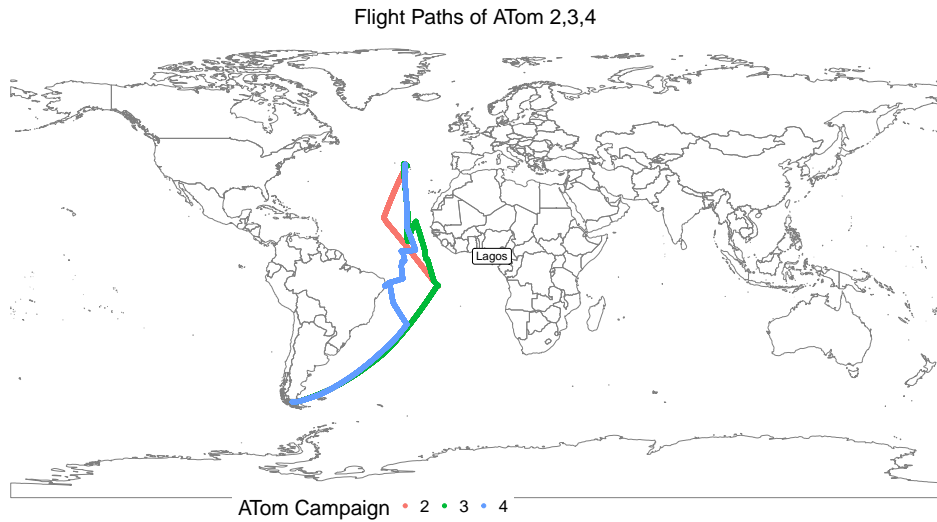


Figure 2.1: Flight paths of Atlantic ATom

Programmable Flask Package (PFP) instrument aboard the DC-8 as well as with data from surface stations close to the ATom flight path. Both of these data sources are considered to be a reliable standard. In ATom 3, the QCLS drifts remained somewhat elusive. As a result ATom 3 QCLS N₂O data is acceptable for use in qualitative source attribution. For flux calculations, and anywhere absolute values are necessary, we are restricted to QCLS data from ATom 2 and ATom 4. Atlantic ATom 4 has less influence from Africa, so apart from some use of ATom 4 data to help interpret ATom 2, we focus our analysis on ATom 2.

2.2 Calculation of Footprints to Assess Surface Influence

Understanding where aircraft observed air was influenced by the surface is useful for analyzing enhancements of chemical species. The end goal of this method is to calculate how much of a hypothetical emission to

the boundary layer should be transported to a point in space and time along the ATom flight track, referred to as a receptor. The boundary layer is the lowest part of the atmosphere in direct communication with the surface, where turbulence due to convection and wind-rough surface interactions result in the air being well mixed with respect to pollutants. A "footprint" is a representation of the notion of surface influence we are pursuing with this method. We combined methods from two different atmospheric transport models to calculate the footprints we used to analyze ATom data: the trajectories calculation from TRAJ3D (Section 2.2.2) and the integration of those trajectories into a footprint from STILT (Section 2.2.1)(*Bowman*, 1993; *Lin et al.*, 2003). We did this in order to save computational resources with the simpler TRAJ3D trajectories, and discuss the STILT method for calculating trajectories as well for comparison.

2.2.1 Overview of the Stochastic Time-Inverted Lagrangian Transport Model

Stochastic Time-Inverted Lagrangian Transport (STILT) is a method for determining the influence of a surface region on a receptor point (*Lin et al.*, 2003). The first step was creating an ensemble of trajectories; the velocity vector at each time step is a combination of the velocity of each hypothetical Lagrangian particle (u), informed by prevailing winds (\bar{u}) given by meteorological data and a stochastic turbulent component (u'). The Hybrid Single-Particle Lagrangian Integrated Trajectory (HYSPLIT) model can provide the mean wind field from either Global Forecast System (GFS) or Global Data Assimilation System (GDAS) meteorological wind fields (*Stein et al.*, 2015).

$$\text{Velocity vector} \quad \overbrace{\boldsymbol{u}}^{\boldsymbol{u}} = \text{Turbulence component} \quad \overbrace{\boldsymbol{u}'}^{\boldsymbol{u}'} + \text{Mean velocity, from HYSPLIT} \quad \overbrace{\bar{\boldsymbol{u}}}^{\bar{\boldsymbol{u}}}$$

The turbulent components of the velocities (\boldsymbol{u}') are calculated as Markov chains, with each time step updated with a Gaussian distributed random variable (λ) scaled with the Lagrangian timescale ($R(\Delta t)$). The parameters λ and Δt are derived from the heat and momentum fluxes in the meteorological fields.

$$\begin{aligned} \boldsymbol{u}'(t + \Delta t) &= \boldsymbol{u}''(t) + \underbrace{R(\Delta t)}_{R(\Delta t)=\exp\left(\frac{-\Delta t}{L_i}\right)} \boldsymbol{u}'(t) \\ \boldsymbol{u}''(t) &= \underbrace{\lambda}_{\lambda \sim N(0, \sigma_i)} (1 - \overbrace{R^2(\Delta t)}^{(1 - R^2(\Delta t))^{\frac{1}{2}}})^{\frac{1}{2}} \end{aligned} \quad (2.1)$$

This gives an ensemble of trajectories. In back trajectory mode, STILT calculates a set of trajectories projecting backwards in time from each receptor (Figure 2.2 A).

2.2.2 TRAJ3D Trajectories

National Oceanic and Atmospheric Administration (NOAA) scientist Eric Ray calculated 245 TRAJ3D modeled trajectories (*Bowman, 1993*) initialized at points randomly distributed around receptors spaced one minute apart along all of the ATom flight tracks¹. The TRAJ3D trajectories are less computationally expensive than STILT ones. For the footprints, or surface

¹<https://espo.nasa.gov/atom/archive/browse/atom/DC8/BdyInfluence>

influence functions, trajectories are computed as in STILT when they enter the boundary layer. The National Center for Environmental Prediction Global Forecast System (NCEP GFS) model and Modern-Era Retrospective Analysis for Research and Applications 2 (MERRA2) model provided the wind fields (NCEP, 2019; Molod *et al.*, 2015). This method of calculating trajectories is less computationally intensive than the STILT approach because it does not have a stochastic component, and the two methods qualitatively agree for ATom data in that the resulting footprints are similar. The stochastic aspect of the STILT trajectory is most important near the source, and the large assortment of TRAJ3D trajectories effectively approximates this turbulence.

Under the TRAJ3D model, trajectories are calculated more simply:

$$x_{t+\Delta t} = x_t + \underbrace{u_t}_{\text{wind field data; NSEC GSF, MERRA2}} \Delta t \quad (2.2)$$

where x_t represents a particle's position at time step t , \mathbf{u}_t is the wind field evaluated at x_t and Δt is the size of the time jump with each iteration.

2.2.3 STILT to Calculate Footprints from TRAJ3D Trajectories

Eric Ray fed the TRAJ3D trajectories into the STILT process for deriving footprints from trajectories. From the trajectories, he calculated an influence function, which represents the fraction of a tracer released at x found at the receptor x_r :

$$I(\mathbf{x}_r, t_r | \mathbf{x}, t) = \frac{1}{N_{tot}} \sum_{p=1}^{N_{tot}} \delta(\mathbf{x}_p(t) - \mathbf{x}) \quad (2.3)$$

Where $\delta(\mathbf{x}_p(t) - \mathbf{x})$ indicates whether a particle launched back in time at the receptor is at location \mathbf{x} with a 1 or a 0, and N_{tot} is the total number of particles. Integrating the influence function with respect to time and each spatial dimension over each boundary layer grid-volume gave the sum of the amount of time each particle spent in each grid-volume of space in the boundary layer.

Assuming that within the boundary layer an emitted tracer is well mixed, we calculated the dependence of the concentration of a tracer at a receptor given an emission in the boundary layer:

A spatial matrix encoding the footprint at a receptor

$$\overbrace{f(\mathbf{x}_r, t_r | x_i, y_j, t_m)}^{} = \frac{m_{air}}{\underbrace{h\bar{\rho}(x_i, y_j, t_m)}_{\text{height and density of boundary layer}}} \frac{1}{N_{tot}} \sum_{p=1}^{N_{tot}} \Delta t_{p,i,j,k} \quad (2.4)$$

Where m_{air} is the mean molar mass of air, h and $\bar{\rho}$ are the height and mean density of the boundary layer, and $\Delta t_{p,i,j,k}$ is the amount of time a particle spends in a particular grid cell. This resulted in a series of footprints going back 30 days at 3 hour resolution for each receptor on the ATom flight track. To calculate the overall influence at a receptor, we summed the series of footprints, resulting in a single footprint at each receptor along the ATom flightpath that encapsulates surface influence over the past month. Each footprint is a 2° latitude-longitude grid, with each grid cell value representing surface influence in units of $\frac{\text{ppm}}{\text{mmol/m}^2/\text{s}}$. It is possible to take the arithmetic

mean for the footprints of several receptors to gain insight into swathes of ATom observations.

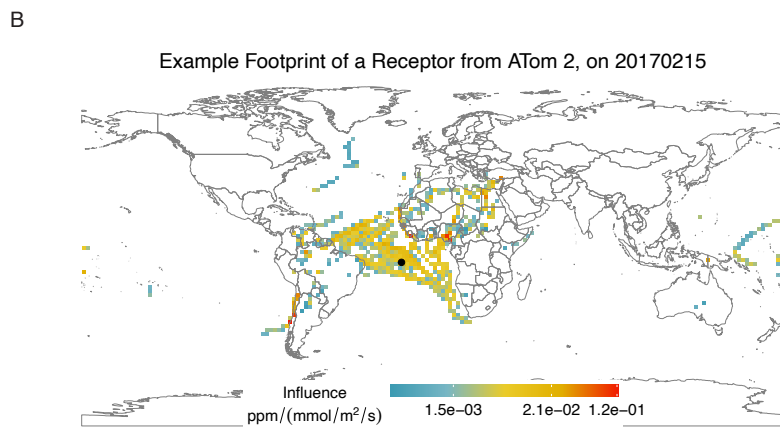
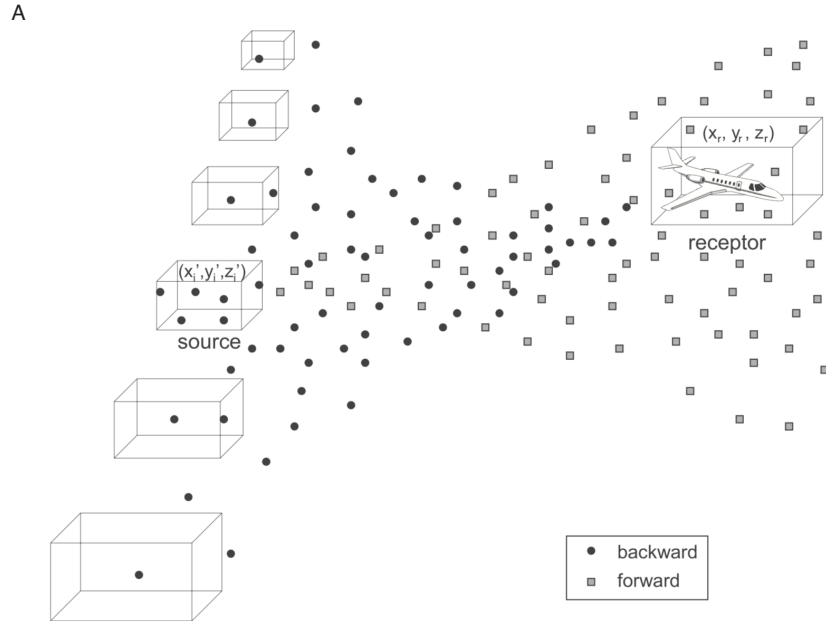


Figure 2.2: **A:** Lin *et al.* (2003)'s schematic of the STILT model. Each black dot represents a particle being transported backwards in time. The boxes represent the grid-volumes within the boundary layer. **B:** An example of a footprint. Footprints represent how much of a enhancement would be observed by the plane given an emission to the boundary layer. In other words, each pixel represents a box in **A**, and a pixel's value is a representation of how often a black dot ends up near the plane, given a set of trajectories.

2.3 Clustering

We wanted to better understand how different sources of N₂O contribute to the overall African emissions and transport budget. In order to do this, it is useful to cluster ATom observations in ways that encapsulate where they were influenced by the surface or their chemistry or a combination of both. The advantage of this method is that it allows us to separately consider different air masses without creating arbitrary or human judgement categories based on altitude, chemical tracers, or continuous profile within the flight.

The Density Based Spatial Clustering of Applications with Noise (DBSCAN) is a popular clustering algorithm that uses closeness defined by Euclidean distance to construct neighborhoods that maximize density (*Ester et al.*, 1996). It is effective at identifying clusters in spatial data that are concave, or generally oddly shaped. It works best in two dimensions.

ATom data has hundreds of chemical variables at each receptor. Each footprint has thousands of grid cells that can each be treated as a dimension. In order to cluster using DBSCAN, we need two dimensional data. T-distributed Stochastic Neighbor Embedding (t-SNE) is a dimension reduction algorithm that maps data in high dimensional space to low dimensional space while preserving closeness between points (*Van der Maaten and Hinton*, 2008). It accomplishes this by mapping the high dimensional data to a Gaussian probability distribution function (PDF), and then a Student's t-distribution with higher probabilities representing higher degrees of closeness.

We wanted to be able to cluster ATom data using where the air was influence by the surface. Each footprint consists of a 2°latitude-longitude

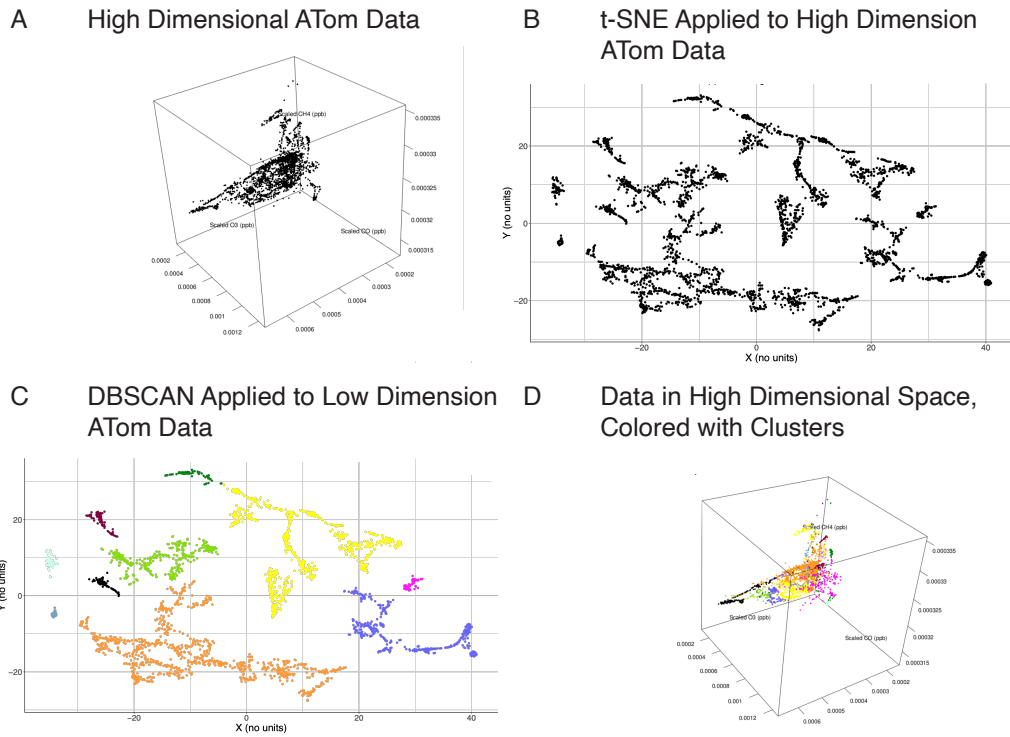


Figure 2.3: **A:** A scatterplot of 3D (O₃, CH₄, CO) ATOm data **B:** A plot of the 3D data after it had been reduced to 2D by t-SNE. **C:** The 2D data colored according to DBSCAN clusters **D:** The original 3D data colored according to DBSCAN clusters, showing spatial cohesion.

grid, with each value representing how much that grid square influenced the receptor. If we consider each grid square as a dimension, we have high dimensional data. We regredded the footprints into 15° squares to reduce the number of starting dimensions by adding all of the smaller grid cells within each larger grid cell in the new regredded footprint.

In summary, to cluster high dimensional data such as the example in Figure 2.3 A, we first reduced the dimension while maintaining continuity of closeness between observations using t-SNE (Figure 2.3 B). We then applied DBSCAN to cluster the 2 dimensional projection of the observations (Figure 2.3 C). Figure 2.3 D shows how this method results in cohesive clusters in the higher dimension space.

T-SNE has a parameter called "perplexity" which controls the shape of the Gaussian distribution. *Van der Maaten and Hinton* (2008) claim that the results of t-SNE are robust to changes in perplexity. This was not the case for our data. DBSCAN has 2 parameters: "epsilon," which controls the maximum distance between points that qualify as connected, and "minPts", which is the fewest number of points that an attempted neighborhood under construction may contain. To select parameters, we iteratively applied the t-SNE/DBSCAN clustering, tweaking all three parameters with the goal of a clustering that: 1) minimized unclustered data and 2) maximized the number of clusters. When applied to ATom chemical and footprint data, the t-SNE/DBSCAN clustering method is robust to changes in the size of a concave subset of the data up to changes in the three parameters perplexity, epsilon, and minPts. This means that if we took a larger subset of ATom data that fully contained a smaller one, any clusters that were in the smaller subset were in the same place in the larger subset once the parameters were adjusted to minimize unclustered data.

We scaled all data to the mean before the clustering algorithms were applied. To select chemical variables, we performed repeated multiple linear regressions as described in upcoming Section 2.4.

2.4 Repeated Multiple Linear Regression with Bayesian Information Criterion for Model Selection and Analysis

One of the joys of the ATom data set is the high number of available variables. There are dozens of trace gasses that can be used as predictors in

modeling, or as the basis of a clustering. Sometimes, as in the case of CO being a clear tracer for combustion, it is known what variables are desired to investigate a certain process. Othertimes, we want to find relationships and patterns in independent variables and we do not have any idea what we are looking for. The goal of the following method is model selection. We wanted to pick the independent variables that produced the linear models with the most skill in predicting N₂O. We did this by finding the variables that most frequently participated in the best of all the possible linear models that it was possible to generate with those variables.

The least squares regression method was first described by the French mathematician Adrien-Marie Legendre, who used it to calculate the paths of comets (*Legendre*, 1806). We calculate multiple linear regressions with every possible combination of independent variables from the set of ATom variables we were interested in. We then ranked those models according to their Bayesian Information Criterion (BIC) (*Sakamoto et al.*, 1986). The BIC is a measure of goodness of fit that penalizes models with more parameters to reduce overfitting. We took the model with the smallest BIC as our winner model. It is also interesting to consider which variables make it into the best models most often. We calculated the fraction of the best 1000 models that contained each variable.

One of the dangers of such a statistical scheme is that by selecting model variables programmatically, rather than through intuition and consideration of the problem, it is possible to violate the least squares assumption of multicollinearity. When attempting to fit a least squares model, if a subset of the model parameters are internally correlated, it violates the multicollinearity assumption of fitting a ordinary least squares linear model, resulting in the slopes of predictors being volatile in response to small changes

in the data.

In order to avoid this, and make our linear models more robust, after selecting the best linear model, we calculated the variable inflation factors (VIF) of that model's independent variables (*Fox and Monette*, 1992). A VIF is a measure of how much an independent variable is affected by multicollinearity. A VIF of 1 indicates that the variable is unaffected by multicollinearity, with higher VIF's meaning worse multicollinearity. The literature is ambiguous on a cutoff for an acceptable VIF, with values ranging from 2 to 10 (e.g. *Craney and Surles* (2002)). We removed any variables in the final model that had a VIF higher than 5.

2.5 Enhancement and Flux Calculation

2.5.1 Modeling the Atmospheric Background of N₂O, CO, and CH₄

We needed an atmospheric background mixing ratio to calculate the N₂O enhancement and flux. We used and assessed two methods for modeling the N₂O background: the first a NOAA Greenhouse Gas Marine Boundary Layer (MBL) product calculated from surface flask data in (*Gonzalez et al.*, 2021), the second calculated from ATom observations in this work.

To derive a background mixing ratio for N₂O, CO, and CH₄, we examined ensembles of HYSPLIT back trajectories to determine where the observed air originated. When the back trajectories intersect the observation of another ATom flight, we can use those observations as a background.

To accomplish this, we interpolated three regions —the Atlantic basin, the Pacific basin, and the Arctic—into curtains of background N₂O, CO, and CH₄ values. Figure 2.4 shows the interpolated background curtains used to calculate the ATom based backgrounds. This figure is interesting because it shows the latitudinal trend of N₂O. The short life time of CO makes pollution plumes, including the African outflow in the Atlantic, clearly discernible. CH₄ also shows a strong latitudinal trend.

We initially attempted to use the mean of the ensemble of TRAJ3D trajectories used to calculate the footprints. However, as can be seen comparing the example ensemble of HYSPLIT trajectories in Figure 2.5 A and the mean TRAJ3D trajectory in Figure 2.5 B, the mean trajectory loses important information: the mean TRAJ3D trajectory would only consider that the air had come from the West, where the HYSPLIT ensemble has a East-erly component. The farther back in time you look, the more a trajectory disperses (Figure 2.5 C). Past two weeks, the trajectories are so diffuse we stopped considering them. We manually assigned each trajectory of each HYSPLIT ensemble at receptors spaced one minute along the ATom flight paths to one of the three background curtains. This produced qualitatively reasonable backgrounds for N₂O, CO, and CH₄, i.e. a background most often less than the observed mixing ratios, and showed that the approach had merit. We then developed a programmatic method to assign Arctic, Atlantic, or Pacific backgrounds to each trajectory based on its endpoint. Two week trajectories that ended between 50°W and 50°E were assigned to the Atlantic. Trajectories that were not within the longitudinal boundaries of the Atlantic and ended North of 45°N were assigned to the Arctic. All other trajectories are assigned to the Pacific. Once assigned to a background curtain, each trajectory in an ensemble was given the background mixing ratio

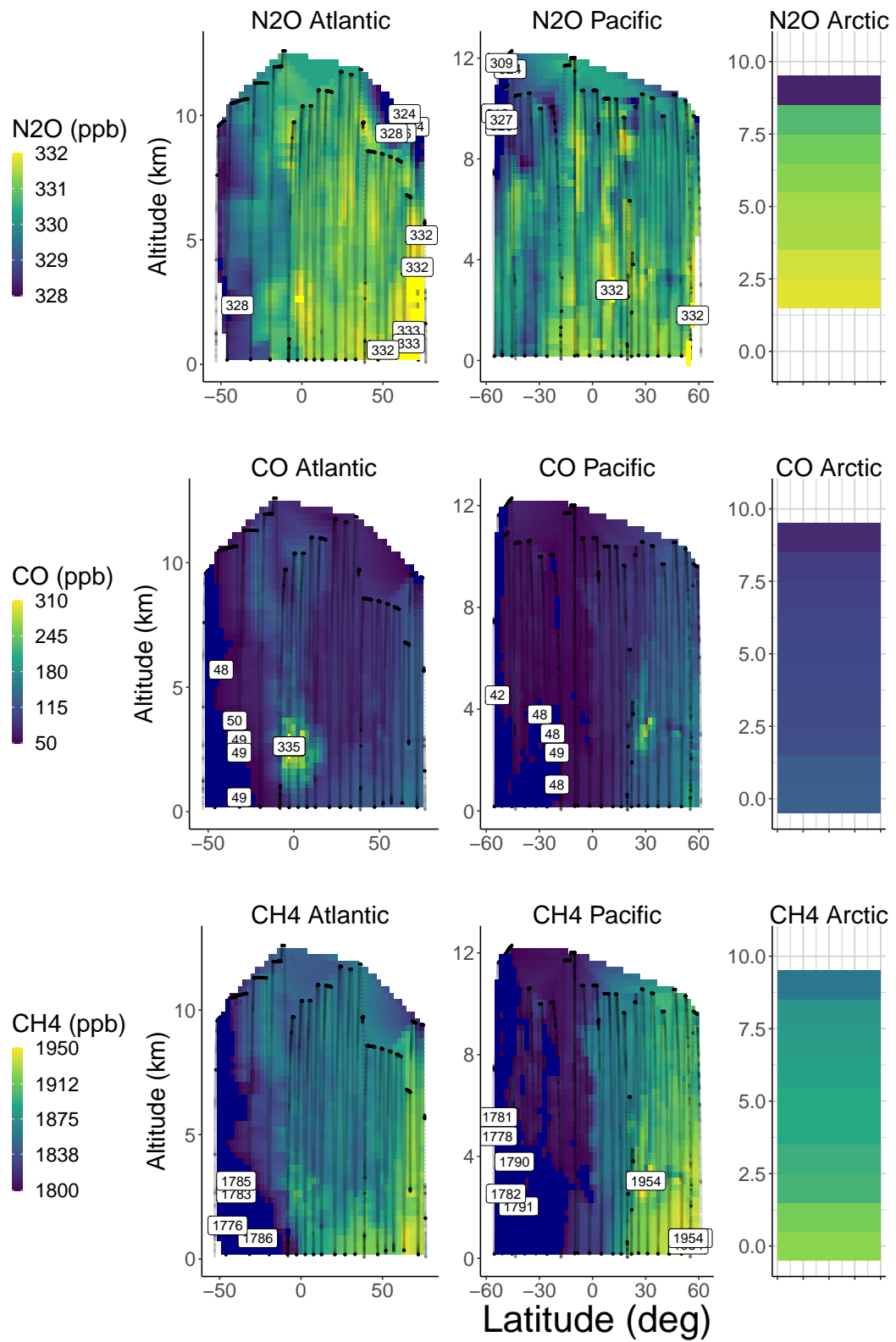


Figure 2.4: Interpolated Atlantic, Pacific, and Arctic background curtains for **A:** N₂O, **B:** CO, **C:** CH₄.

from the cell in the background curtain nearest to the end point of the trajectory. Finally, we took the arithmetic mean of the background mixing ratios of the trajectories in each receptor's ensemble to give that receptor a background.

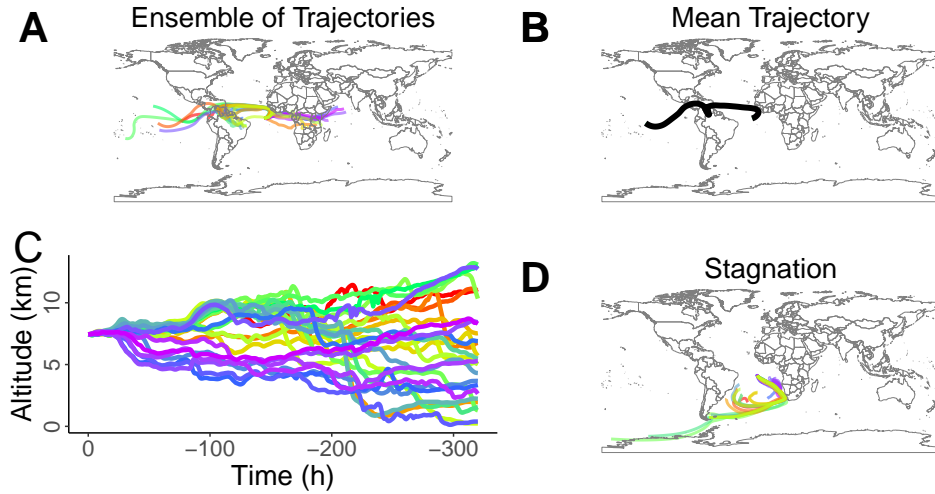


Figure 2.5: **A:** Example of an ensemble of HYSPLIT trajectories. Color differentiates different trajectories in the 27 member ensemble. **B:** Example of a Mean TRAJ3D Trajectory. **C:** Example of a HYSPLIT trajectory ensemble trapped in the boundary layer.

One issue with the ATom background method is low altitude receptors entering the boundary layer, an example of which can be seen in Figure 2.5 D. Back trajectory models such as HYSPLIT struggle to model air in the boundary layer. This may result in the modeled background being inverted with the observed mixing ratio, and is especially noticeable in low altitude CH₄ data (Figure 2.6 B). Because we know the QCLS CH₄ data is accurate, we resolved this by using the MBL background in calculating all enhancements whenever the CH₄ is inverted. Using a Marine Boundary Layer background makes sense at these receptors because they are low altitude over the ocean. Our final ATom trajectory background model used to calculate enhancements and fluxes is a hybrid that uses the MBL as a fall-

back whenever the HYSPLIT trajectories struggle, most frequently at low altitudes. See Figure A.2 - Figure A.7 in the appendix for all of the background profiles, corrected with the CH₄ inversion rule.

Figure 2.6 shows observed mixing ratios, and MBL and ATom trajectory modeled background mixing ratios for N₂O, CO, and CH₄. Both of these methods have strengths and weaknesses. The ATom trajectory background allowed us to compare ATom QCLS measured background mixing ratios with other ATom QCLS mixing ratios to calculate enhancements. This circumvented concerns about the QCLS, drifts in which would propagate into the calculated flux if the background mixing ratio came from a non-QCLS source. In addition, the ATom trajectory modeled background has more detail than the MBL derived background, and is more specific to regional enhancement. In our application, it gives insight into what portion of the N₂O enhancement is from African emissions, versus advection from the boundary. However, because it is focused on regional enhancements, its effectiveness wanes when applied to more global air that saw the surface farther in the past. This is reflected in the background mixing ratio profiles from outside the African outflow, which can be inverted with the ATom observed value, and cannot be considered meaningful (Figure A.2 - Figure A.7). ATom trajectory modeled backgrounds are most effective for CO because its short lifetime means that all observable emission enhancements are have been transported a short distance.

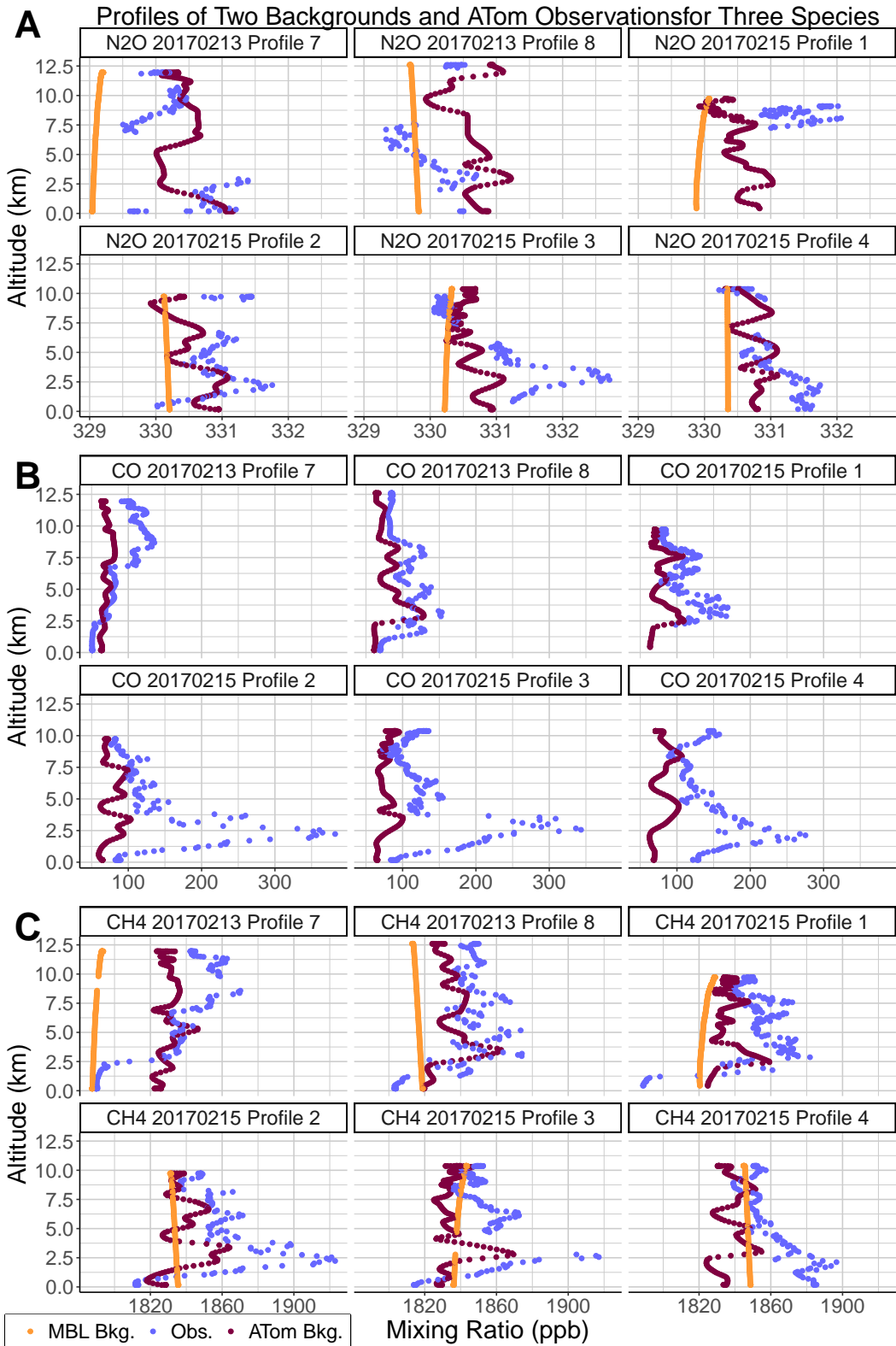


Figure 2.6: Profiles of ATom observed mixing ratios and background mixing ratios modeled with the MBL and with ATom observations and trajectories for **A:** N₂O, **B:** CO, and **C:** CH₄.

One point emerges clearly: significant portions of the Atlantic ATom 2 observed vertical structure of N₂O mixing ratios represent advection influence rather than African emissions. However, we can also see notable African emissions. This discussion underscores the difficulty of extracting the African signal from observations of N₂O due to its long lifetime and low variance mixing ratio. To paraphrase George Box², "all models of the atmospheric N₂O background are wrong, but some are useful."

2.5.2 Flux Calculation

Enhancement of a species (Δ_{species}) is the difference between the ATom observed mixing ratio and the modeled "background" mixing ratio, defined as the inflow from the boundary of the of the Atlantic region as described above. We calculated flux by multiplying the zonal wind component (u), measured by the DC-8, by the number density of the enhancement. For the subset of Atlantic ATom focused on the African outflow, only observations with positive easterly zonal wind are considered (Figures A.1, A.9). We then interpolate flux values along the flight path onto a latitude-altitude grid Figure A.8, multiply each grid cell's flux value by its area (Equation 2.5), and sum to calculate the total N₂O source observed by ATom in units

²The popular misquote "all models are wrong but some are useful" models Box's comment in *Empirical Model-Building and Response Surfaces*: "Remember that all models are wrong; the practical question is how wrong do they have to be to not be useful" (Box and Draper, 1987).

of mass per time (Equation 2.6).

$$\text{area}_{\text{cell}} = \Delta \text{altitude}_{\text{cell}} * (111,132.95 - 560 * \cos(2 * \text{Lat}_{\text{cell}} * (\pi/180))) \Delta \text{Lat}_{\text{cell}}$$

(2.5)

$$\text{Flux}_{\text{species, outflow}} = \sum_{\text{outflow cells}} \text{area}_{\text{cell}} * \Delta_{\text{species, cell}} * u_{\text{cell}}$$

(2.6)

2.6 Convolving Emissions Fields to Compare with ATom Values

To calculate a modeled enhancement at a receptor along the flight path due to a given emissions field ($\Delta_r(E)$), with grid cell values of flux in units of $\frac{\text{mol}}{\text{m}^2 \text{s}}$, the matrix of the emissions field (E) is multiplied by the footprint at that receptor (F_r) (Equation 2.7).

$$\Delta_r(E) = E * F_r$$

(2.7)

To compare our values with the literature, we calculated the N₂O enhancements generated by emissions fields from *Tian et al.* (2020). We also calculated the convolutions of other emissions fields. The Emission Database for Global Atmospheric Research (EDGAR) is a 1°gridded emissions product for CO and CH₄ among other trace gasses based off of land use emissions factors (*Olivier et al.*, 1994). The Global Fire Emissions Database (GFED) is a .25°global fire specific emissions field with data for N₂O, CH₄ and others (*Randerson et al.*, 2017). The Diffuse and Inefficient Combustion Emissions in Africa (DICE-Africa) is an anthropogenic combustion emis-

sions field for Africa that divides emissions of CO and other gasses into different categories such as motor fuel and fuel wood burning (*Marais and Wiedinmyer, 2016*).

The Moderate Resolution Imaging Spectrometer (MODIS) is an instrument on both the Terra and Aqua satellites that, among other things, uses data in the infrared spectrum to produce an open fire count data product (*Giglio and Justice, 2015*). We aggregated these data into a map where each pixel represents fires per square kilometer over the month prior to each ATom campaign.

2.7 Statistics, Math, and Code

We used the bootstrap method, under which results are repeatedly re-sampled with a sample size of the number of results, to calculate all confidence intervals in this work (*Efron, 1979*). To interpolate both univariate (ATom trajectory background values) and 3 dimensional data (background curtains) we used Akima's methods (*Akima, 1991, 1996*). We wrote all code and did all calculations in R version 4.0.2 (*R Core Team, 2020*). Code can be found at <https://github.com/BlueGrisGris/ethans-thesis>.

Chapter 3

Results and Discussion

Performing the clustering method described in Section 2.3 on Atlantic ATom 2, (flights 20170215, 20170213), ATom 3, (flights 20171014, 20171019, 20171020), and Atlantic ATom 4 (flights 20180512, 20180514, 20180517) separately results in 8 clusters in Atlantic ATom 2, 12 clusters in ATom 3, and 8 clusters in ATom 4 (Figures A.10-A.12). In ATom 2, clusters 4, 5, and 6, and in ATom 4, clusters 2, 4, and 5 roughly align with the Easterlies (Figure A.1, A.13, A.14). We refer to these clusters as the African outflow. ATom 2 Cluster 4 shows the strongest influence from Lagos.

3.1 Combustion Sources of N₂O and the African Outflow

In the ATom 2 African outflow, N₂O ranges from 328.8 ppb to 332.7 ppb with a mean of 330.6 ppb. Assuming an MBL background we find an average enhancement of 0.84 ppb, and a maximum enhancement of 3.06 ppb, and assuming an ATom trajectory background we find an average enhancement of 0.45 and a maximum enhancement of 1.97 ppb. Much of the variation seen in N₂O coincides with variation in CO within the African outflow (Figure 3.1 A). This suggests a combustion source, or colocation with combustion. The strong correlation between CO and HCN through all of the ATom 2 data (Figure 3.1 B) suggests that most of the combustion is

biomass burning, either forest fires, agricultural fires or other anthropogenic biomass burning (e.g. charcoal). As one would expect, Africa is the focus of the modeled land influence on the African outflow (Figure 3.1 C).

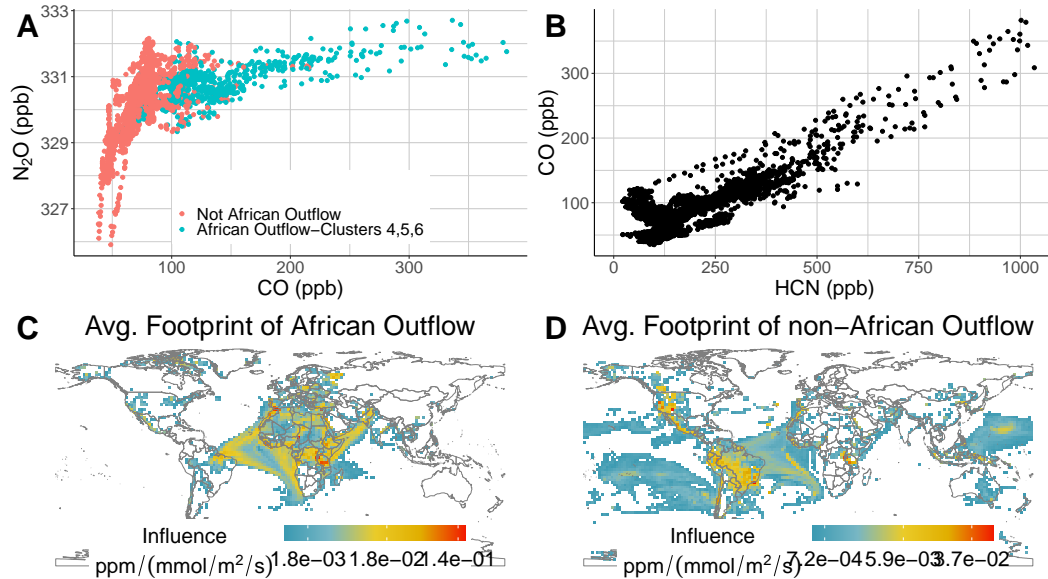


Figure 3.1: A: Scatterplot of ATom 2 data, N_2O against CO mixing ratios, with observations in the African outflow clusters colored blue, showing a correlation with CO, implying a connection with combustion. B: Scatterplot of CO vs. HCN mixing ratios, where the correlation indicates that much of the combustion is biomass burning. C: Average footprint of the ATom 2 African outflow D: Average footprint of the non-African outflow

Outside of the African outflow, N_2O mixing ratios range from 325.9 ppb to 332.2 ppb with a mean of 330.0 ppb. Assuming an MBL background we find an average enhancement of 0.711 ppb N_2O and a maximum enhancement of 3.11 ppb N_2O . Assuming an ATom trajectory modeled background, we find an average enhancement of 0.475 ppb N_2O and a maximum enhancement of 2.22 ppb N_2O . CO variations are not strongly correlated with variation in N_2O in the non-outflow clusters (Figure 3.1 A). This suggests that non-combustion processes such as Stratosphere–Troposphere Exchange and soil emission sources have more control. It could also be a consequence of the non-African outflow air having not seen the surface for

a long time, resulting in short-lived CO not making it to the NASA DC-8 alongside the pollution. Figure 3.1 D shows the lack of African influence on these clusters, and influence from the Pacific and South America.

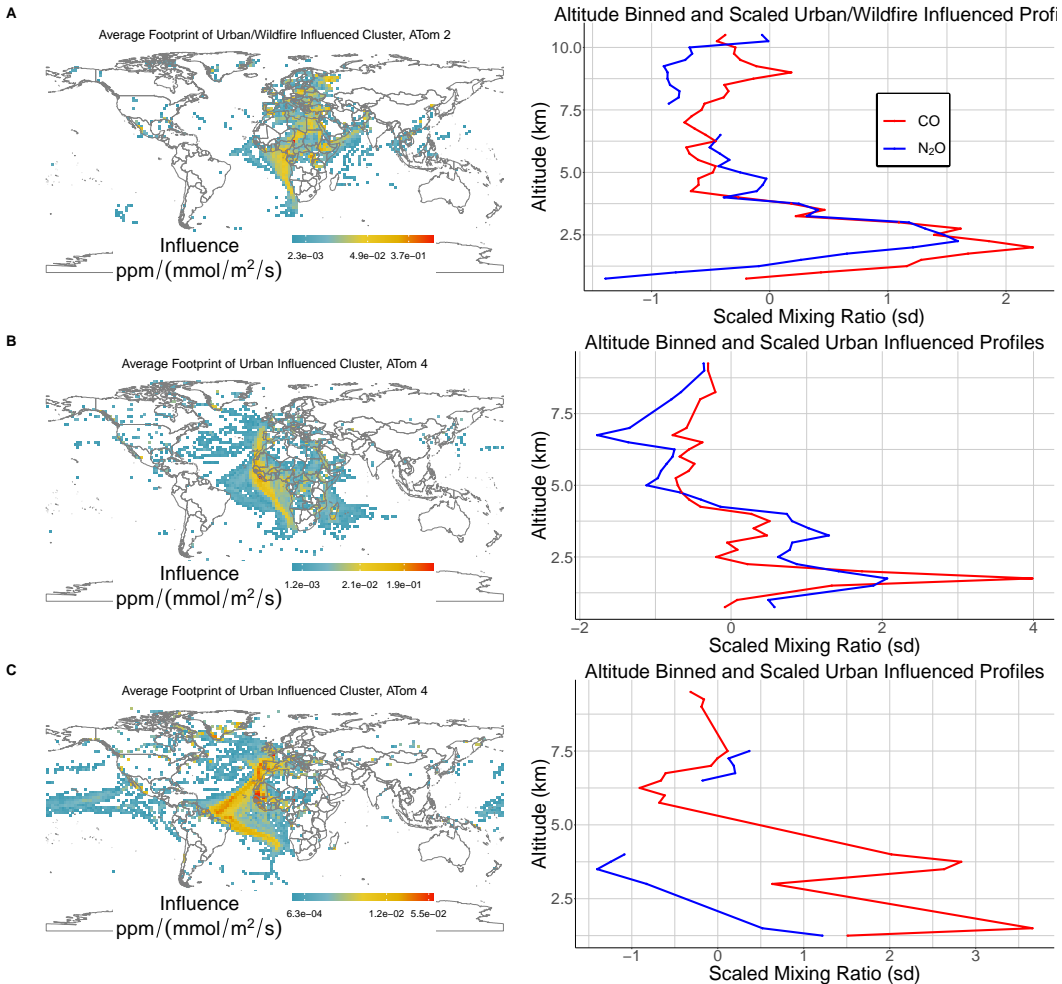


Figure 3.2: **A:** Binned N₂O and CO profiles (right) and average footprint (left) of Cluster 4 of ATom 2 African outflow observations that is influenced by co-located wildfires and cities. **B:** Same as A for Cluster 4 ATom 4, only influenced by cities. **C:** Same as A for Cluster 2 & 3 ATom 4, only influenced by wildfires.

Atlantic ATom 2 and ATom 4 both observed concurrent CO and N₂O enhancements in the easterly outflow from Africa. Within the ATom 2 African outflow, N₂O is correlated with CO in Cluster 4, which is influenced strongly by West Africa, including Nigeria and the megacity of Lagos

Table 3.1: Correlation coefficients of N_2O and CO in the clusters in Figure 3.2. The p-value is for the null hypothesis of $R^2 = 0$

Cluster	R^2	p-value; $H_0: R^2 = 0$
ATom 2 Urban/Wildfire, (Figure 3.2 A)	0.737	$2.22 * 10^{-16}$
ATom 4 Urban, (Figure 3.2 B)	0.745	$4.19 * 10^{-16}$
ATom 4 Wildfire, (Figure 3.2 C)	0.061	0.759

(Figure 3.2 A). During ATom 2, intense forest fire activity occurred too close the urban center of Lagos to determine the primary combustion contributor to the N_2O enhancement (Figure 3.3). During ATom 4, the forest fires were located in West Africa and Southeast Africa. ATom 4 Cluster 2 and 3's average footprint overlaps forest fire activity, but shows no correlation between N_2O and CO (Figure 3.2 C). ATom 4 Cluster 4, which shows some influence from Lagos, has N_2O correlated with CO (Figure 3.2 B). Table 3.1 shows the correlations between N_2O and CO for all clusters in Figure 3.2.

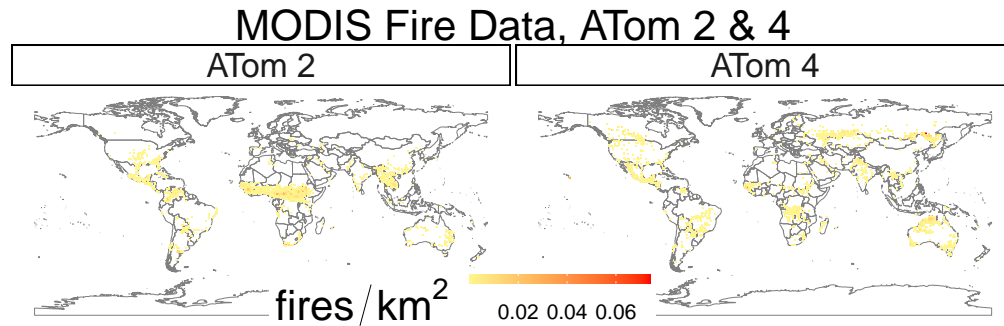


Figure 3.3: Open fire density aggregated over the month prior to each ATom calculated from MODIS satellite data. ATom 2 sees high fire activity near Lagos as well as the entire Sahel. ATom 4 sees less overall fire activity than ATom 2, mostly in Western Africa and the Congo.

3.1.1 Interhemispheric Transport of N₂O

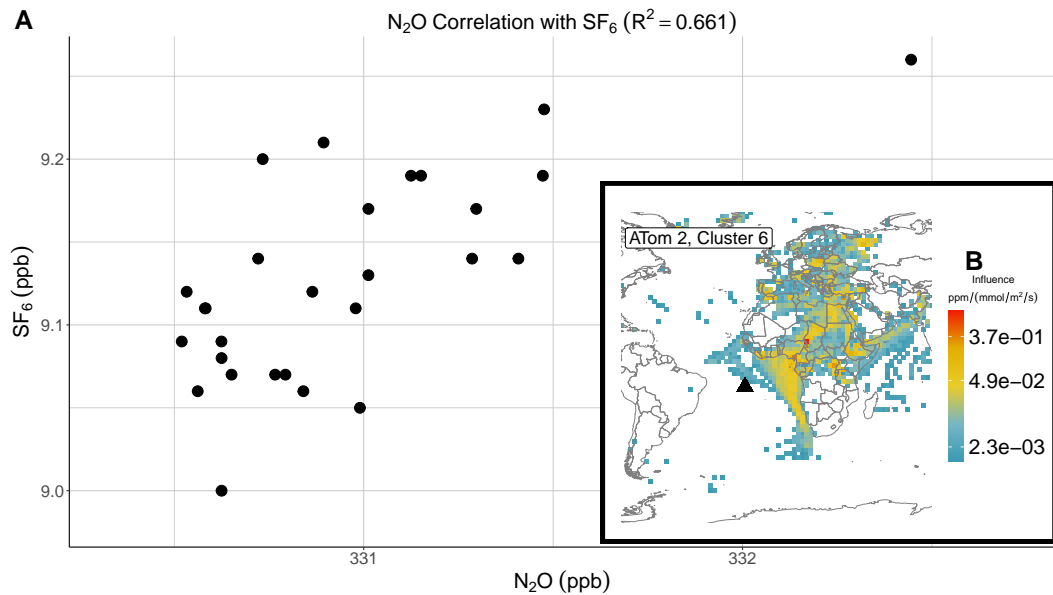


Figure 3.4: **A:** Scatterplot of ATom 2, Cluster 6 observed mixing ratios of N₂O in ppb and SF₆ in ppb showing the correlation of $R^2 = 0.661$. **B:** Average footprint of profiles 2 and 4 in ATom 2 showing European influence.

This suggests that most of the N₂O enhancement observed by ATom 2 comes from urban sources. Stronger N₂O emissions from the cities than the wildfires could represent hotter human fossil fuel and biomass combustion more frequently having the energy to break the strong bond in molecular nitrogen¹. Combined with the conclusion from Figure 3.1 B that much of the combustion is from biomass burning, we can interpret this as a human wood and charcoal burning source of N₂O concentrated in Lagos.

In ATom 2, the cluster with urban associated N₂O is also influenced by Europe (Figure 3.2 A). The N₂O peak observed in ATom 2 profiles 2 and 3 is correlated with sulfur hexafluoride (SF₆) mixing ratios (Figure 3.4 A). The only source of SF₆ is industrial activity, resulting in its mixing ratio

¹This idea arose in an interesting conversation with Prof. Ann Pearson

being a proxy for how recently air was in the boundary layer in the Northern midlatitudes (Waugh *et al.*, 2013). A significant portion of the combustion derived N₂O pollution plume putatively from Africa has a Northern Hemisphere origin, likely Eastern Europe (Figure 3.4 B). This agrees with convolved EDGAR and *Tian et al.* (2020) enhancements, which estimate the N₂O enhancement being split between European and African origin (Figure 3.7).

3.1.2 Possible Heterogeneous Chemical Source of N₂O

Currently, N₂O budgets do not account for a heterogeneous N₂O source. Figure 3.5 show the relationships between species involved in the redox chemistry proposed by *Wang et al.* (2020) and *Martin et al.* (1981) to generate both sulfate PM and N₂O. ATom did not have an instrument to measure HONO, so we omit it. We compare N₂O mixing ratios with the mass of BC and sulfate aerosols, as well as NO_x in Figure 3.5, restricted to data within the African outflow. We also restrict this analysis to observations with positive BC, because *Wang et al.* (2020) observed high BC in their analyzed Beijing haze event. We also reason that positive BC indicates that the air has not been subsequently cloud processed, which would remove SO₄²⁻. In this polluted subset of the data, we find strong correlations between N₂O and the proposed inputs and products of *Wang et al.* (2020)'s proposed mechanism (Figure 3.5). Assuming that all of the observed increase in sulfate PM 1 is due to the heterogeneous oxidation process, and that all of the generated sulfate PM 1 survives transport from where it was created to where it was observed by the plane, allows us to calculate an upper limit on the amount of N₂O that could have been produced. In Figure 3.5 D, there is an overall increase of approximately 4.5 ppb sulfate PM, which would correspond to an increase of approximately 1.5 ppb N₂O, assuming the theoretical 1:3 N₂O:SO₄²⁻ ratio from *Wang et al.* (2020). In the same figure, there is an increase of approximately 1.5 ppb N₂O.

We do not find conclusive evidence of N₂O production via heterogeneous chemistry. We also cannot exclude the possibility that it is a small but relevant contributor to N₂O enhancements in urban-industrial pollution rich in sulfur. The correlations between the germane species we find in the

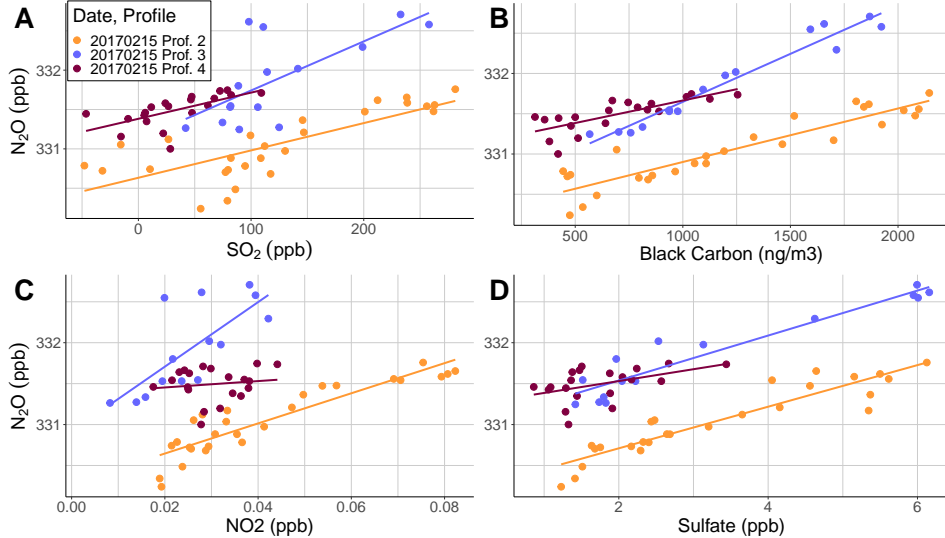


Figure 3.5: Scatterplots showing correlations between species relevant to theoretical heterogeneous N_2O pathways. Data are restricted to observations with positive BC in the African outflow.

African outflow are certainly suggestive. Our more general analysis of N_2O enhancements outside of the African outflow in upcoming Section 3.2 also hint at a sulfur- N_2O connection.

3.2 Analysis of Non-African Outflow N_2O Enhancements

Although the focus of this work is the African outflow, we also consider the non-African outflow clusters in ATom 2. We use the repeated multiple linear regression method to gain insight into the trace gasses that best predict N_2O .

In Cluster 1, APO, CH_4 , and O_3 stand out as important predictors of N_2O mixing ratios. Cluster 1 is not spatially connected (Figure A.13), containing high altitude observations at high northern latitudes, and low altitude observations just south of the Equator. O_3 's importance as a N_2O

predictor could be indicative of Stratosphere-Troposphere exchange in the high altitude piece of Cluster 1, while APO could be related to an oceanic upwelling region N₂O source or a biomass burning source.

Cluster 2's strongest represented variables are CH₄, SO₂, and BC (Figure 3.6). Cluster 2 also shows relatively strong representation by CO amongst the best fit linear models, in comparison to the other non-African outflow clusters. The average footprint of Cluster 2 (Figure A.10) shows influence from Southeast Australia, which was affected by wildfires during ATom 2 (Figure 3.3), and has a significant source of urban-industrial pollution from the Sydney region. The higher than expected CO could be due to these sources. The low overall CO is likely due to CO's short lifetime and a longer travel time from Australia than Africa. SO₂'s relevance suggestively points towards more heterogeneous chemistry.

Cluster 3 has few observations (Figure A.13) and no outlier predictors of N₂O (Figure 3.6). Cluster 7's receptors are low altitude over the Atlantic, North of the Equator. It is influenced by North America (Figure A.10), and its best represented variables are O₃, nitric acid, and SO₂ (Figure 3.6), again suggesting a possible heterogeneous source, potentially due to North American pollution.

In Cluster 8, APO, H₂O₂, NO_y, and PAA dominate as parameters of the cohort of N₂O predicting models (Figure 3.6). The average footprint of Cluster 8 shows influence from (Figure A.10) Western Europe, Eastern Asia, and Indonesia, as well as oceanic influence, though not over a strong upwelling region. The Cluster 8 N₂O predictive tracers other than APO are all associated with sunlight processing of urban pollution. The different regions of land influence all could contribute urban-industrial pollution.

Consideration of observations of air from farther afield from the

ATom 2 African outflow is important because it shows that urban-industrial pollution sources frequently drive N₂O mixing ratios even when they are distant. We would expect natural and agricultural emissions to be the most important sources of N₂O, but we cannot isolate them.

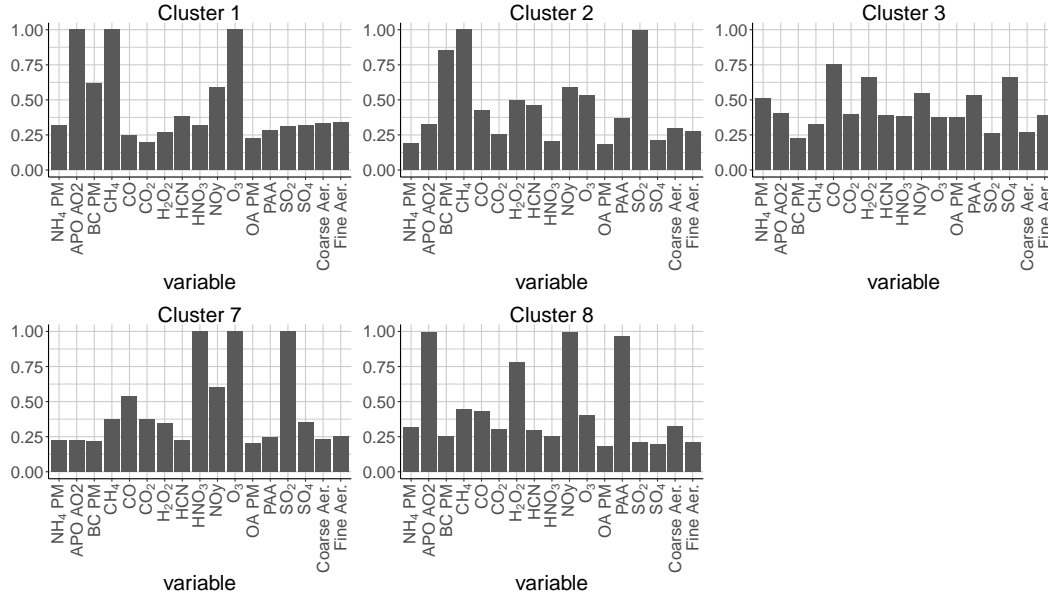


Figure 3.6: For non-African outflow: the fraction of each independent variable found in the 1000 multiple linear regression models with the lowest BIC.

3.3 Comparison with *Tian et al. (2020)*

We compare the average profiles of convolved *Tian et al. (2020)* N₂O enhancements with two modeled ATom N₂O enhancements. *Tian et al. (2020)* predicts that most of the European emitted N₂O would be observed by ATom at low altitude, below approximately 4 km (Figure 3.7 A). In Figure 3.7 B, our two modeled ATom N₂O enhancements agree at low altitudes, below approximately 4 km. At higher altitudes, the MBL modeled N₂O enhancement is higher. The ATom trajectory model is more specific to regional emissions; where the ATom trajectory model and the MBL model agree, most of the N₂O enhancement is due to nearby emissions. We interpret the higher altitude discrepancy as N₂O delivered by advection. This is a qualitative difference between our understanding and *Tian et al. (2020)*'s about the structure of African outflow N₂O enhancements and their influence from outside Africa.

We explore the distributions of the difference $\Delta \text{N}_2\text{O} = \text{Tian et al. (2020)} - \text{ATom modeled N}_2\text{O enhancement}$. The residuals calculated with our ATom trajectory background have a wider distribution than those calculated with the MBL background (Table 3.2). The ATom trajectory background model calculated residuals are right skew, where the MBL residuals have a symmetrical distribution (Figure 3.8 A). This reflects the ATom trajectory background model being biased high, as discussed in Section 2.5.1, as well having an additional source of variance in the trajectory background model. For these reasons, we only considered the residuals calculated with the MBL background when broken down by cluster in Figure 3.8 B).

We applied the repeated multiple linear regression method from Section 2.4 to gain insight into what processes are associated with differ-

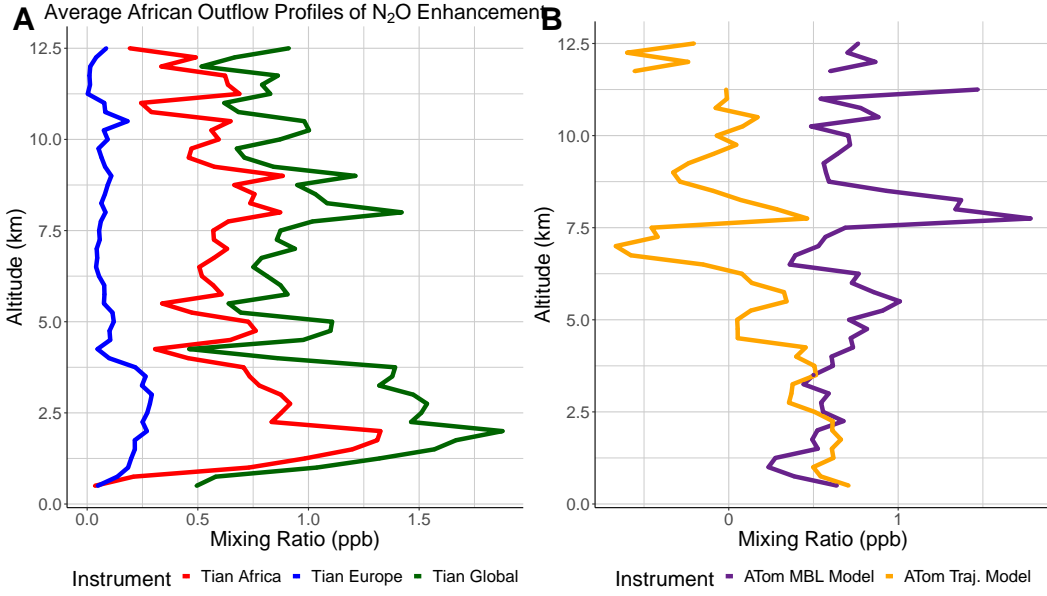


Figure 3.7: Altitude binned profiles of **A**: convolved *Tian et al.* (2020) and **B**: ATom modeled N_2O enhancements taken from the ATom 2 African outflow. Structurally, *Tian et al.* (2020) would expect ATom to see more European influence at low altitude, while we model regional influence at low altitude and advected European emissions at high altitude.

ences between modeled ATom N_2O enhancements and *Tian et al.* (2020)'s modeled N_2O enhancements. When we attempted to predict the difference $\Delta\text{N}_2\text{O}$, we found that different variables are better predictors in different ATom 2 African outflow clusters. (Figure 3.9).

Cluster 4, the cluster most directly influenced by Lagos, has a negative mean $\Delta\text{N}_2\text{O}$ and is right skew (Figure 3.8, Table 3.2). The best predictors of $\Delta\text{N}_2\text{O}$ are BC, CH_4 , and PAA. CO_2 , HCN, and SO_2 also seem relevant. These tracers somewhat align with the profile of urban biomass burning we described in Section 3.1. We tentatively interpret this as our ATom modeled N_2O enhancements seeing the heavily concentrated urban biomass burning source, which is less expressed in *Tian et al.* (2020)'s bottom up model. The skew could be due to outlier ATom observations of air with low background N_2O transported from the South Atlantic.

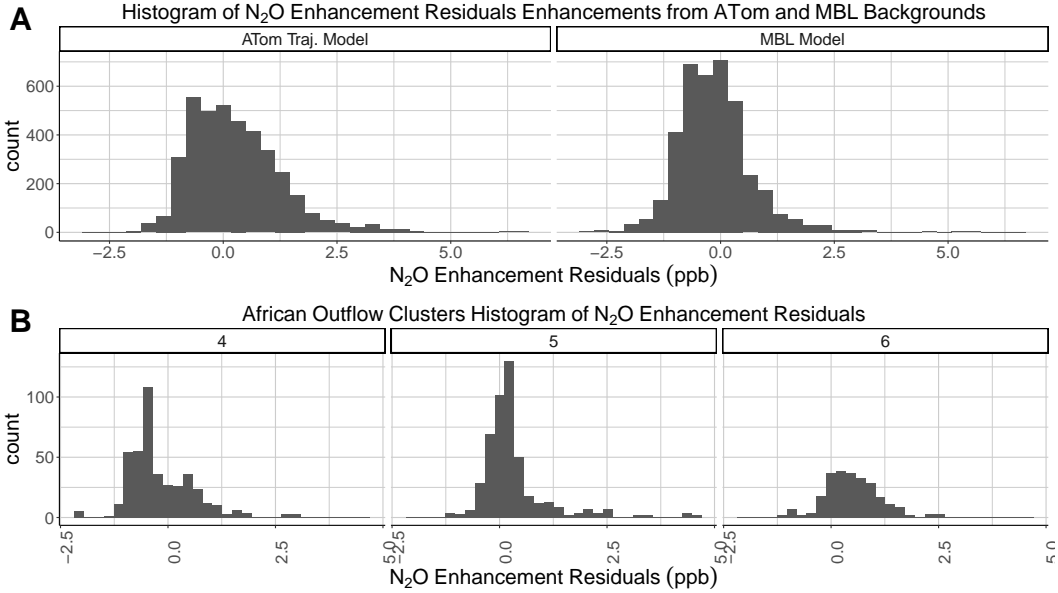


Figure 3.8: The distributions of the difference *Tian et al. (2020)* - ATom calculated enhancement for **A**: the African outflow enhancements calculated using ATom trajectory background and using the MBL background. **B**: Distribution of the residuals for each African outflow cluster, calculated with the MBL background.

In Cluster 5 $\Delta \text{N}_2\text{O}$ is right skew as well, but has a positive mean. BC and APO again are the best predictors of $\Delta \text{N}_2\text{O}$. In Cluster 6, $\Delta \text{N}_2\text{O}$ has a wider spread, and is left skew. This spread and skew could represent high outlier N_2O mixing ratios influenced by Lagos and Nigeria (A.10). The important predictors of $\Delta \text{N}_2\text{O}$ in this cluster are BC, APO, CH_4 , and NO_y . The BC and possibly the APO map onto urban biomass burning emissions, suggesting that ATom observed more of N_2O from this process than expected by *Tian et al. (2020)*. CH_4 's predictive ability could indicate *Tian et al. (2020)* underestimates the N_2O source of Lagos' vigorous oil and gas industry.

Overall, tracers of combustion pollution predict difference between ATom and *Tian et al. (2020)* across all African outflow clusters. This suggests that *Tian et al. (2020)* does not fully model concentrated anthropogenic biomass burning N_2O sources.

Table 3.2: Summary statistics of ΔN_2O = (Tian Modeled Enhancement - ATom Modeled Enhancement)

Data/Model	Mean(ΔN_2O)	sd(ΔN_2O)	95% C.I. ΔN_2O
African Outflow/ATom Traj.	0.241 ppb	1.01 ppb	(0.189, 0.244) ppb
African Outflow/MBL	-0.124 ppb	0.839 ppb	(-0.203, -0.152) ppb
Cluster 4/MBL	-0.169 ppb	0.772 ppb	(-0.252, -0.106) ppb
Cluster 5/MBL	0.318 ppb	0.817 ppb	(0.181, 0.292) ppb
Cluster 6/MBL	0.497 ppb	0.643 ppb	(0.375, 0.517) ppb

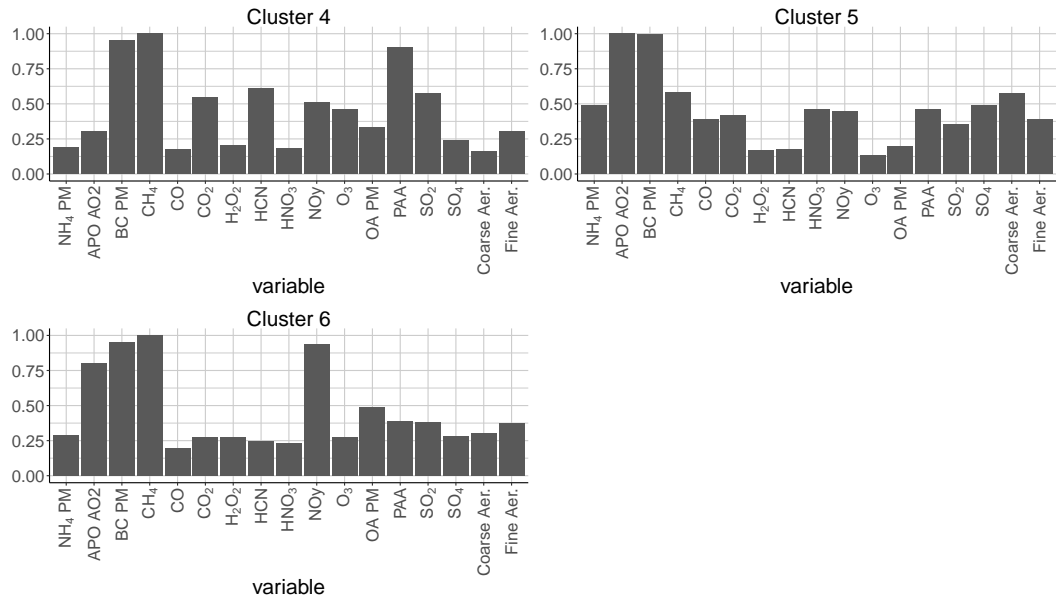


Figure 3.9: For African outflow ΔN_2O = ATom modeled N_2O enhancement - Tian et al. (2020) enhancement: the fraction of each independent variable found in the 1000 multiple linear regression models with the lowest BIC

3.4 Quantifying Flux

We calculated N_2O , CO, and CH_4 , fluxes for Atlantic ATom (Figure 3.10). ATom N_2O MBL flux exceeds Tian et al. (2020)'s bottom up estimates of African flux. ATom trajectory modeled N_2O flux is less than than Tian et al. (2020)'s African estimate, which could be due to the ATom trajectory model being specific to a smaller region than the whole African continent. Tian et al. (2020) bottom up estimates also predict that roughly one half to

two thirds of the flux in the African outflow comes from Africa.

Flux calculated from convolved DICE values suggests a strong input external to Africa, while FINN suggests a primarily African input. ATom CO flux agrees best with DICE total flux values. This further supports the hypothesis that a significant portion of the N₂O in the African outflow is influenced by surface emissions in Europe. CH₄ flux calculated from the ATom MBL model is less than that predicted by EDGAR. Both MBL and ATom backgrounds result in CH₄ fluxes that are less than those predicted by convolved EDGAR values.

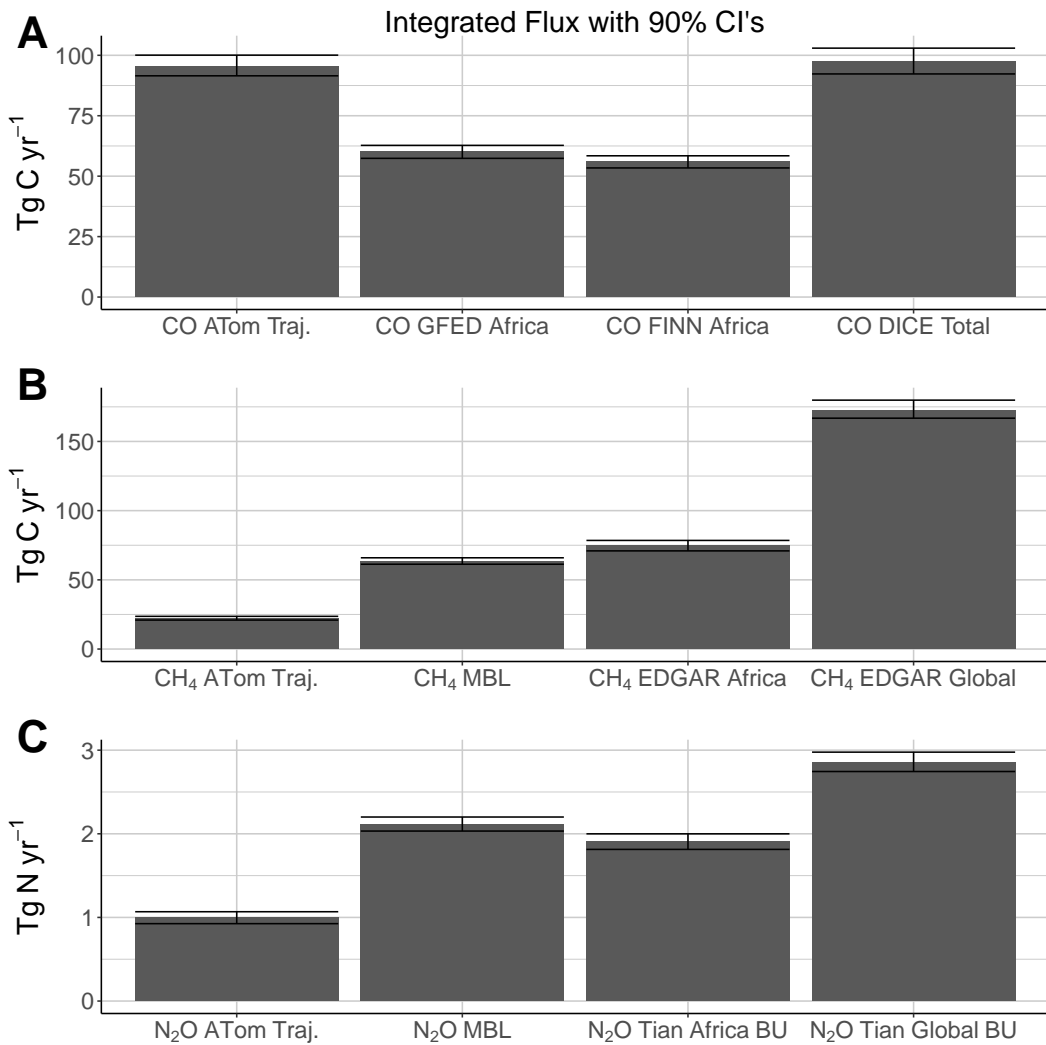


Figure 3.10: Comparison of modeled total fluxes for **A:** N₂O, **B:** CO, **C:** CH₄. Confidence interval bars represent the middle 90% quantile of the bootstrapped means. These CI's only capture variance in internal to our modeled flux. They do not account for uncertainty in the models of the background described in Section 2.5.1, which could represent an additional factor of 2.

Chapter 4

Conclusion

Atmospheric N₂O is increasing due to human activity, which bears consequences to climate that impact all of us. This work evaluates N₂O enhancement in the African outflow observed by Atlantic ATom. We improved understanding of the relative importances of regional emissions and advection to the vertical structure of N₂O. Although HCN data suggest that African outflow N₂O enhancement is associated with biomass burning, our cluster analysis does not find a strong wildfire N₂O enhancement. Instead, we find indications that use of wood and charcoal as fuel, and urban-industrial sources with high sulfur content may be the most important sources of N₂O to the African outflow. We also find that a significant portion of the African outflow N₂O enhancement is due to air transported from the Northern hemisphere, specifically Europe.

We investigated the potential of a source of N₂O in the heterogeneous chemistry of urban pollution by examining the correlations of N₂O, SO₂ and SO₄²⁻. These findings extend the work of Wang *et al.* (2020) from local ground based measurements to regional airborne observations. Within the African outflow, our modeled enhancements largely agree with those modeled by Tian *et al.* (2020). The best predictors for the difference between our modeled enhancements and their modeled enhancements are tracers for the anthropogenic biomass burning processes we investigated. Outside the African outflow, we find evidence that urban-industrial pollution trans-

ported from Australia, Europe, East Asia, and North America drives N₂O enhancements. In this old pollution, we also find suggestions that heterogeneous sulfur chemistry is connected to N₂O. The key lesson in this work is that understanding transport is vital to understanding regional N₂O.

This work highlights the challenge of investigating N₂O emissions. N₂O enhancements are small (\approx 1-3 ppb) in comparison to the precision of instruments (\approx 0.5 ppb), resulting in a low signal-to-noise ratio. *Thompson et al.* (2014) also comment on the issue of signal to noise ratio in observing atmospheric N₂O. In the future, understanding of N₂O could be furthered by improvements in measurement technology.

We do not successfully isolate a terrestrial or oceanic source of N₂O. This is notable because these sources should be the largest. In the non-African outflow clusters, APO is with N₂O, which could be a tracer of atmosphere-ocean exchange. However, APO may also be affected by biomass burning. Soil N₂O emissions may be hard to identify for a combination of the following: we do not have a unique long lived tracer of soil nitrication/denitrification, and our footprints are to diffuse to geographically separate locations where soil emissions dominate from urban centers.

Africa has the least constrained N₂O budget in *Tian et al.* (2020) because it is least studied region. Boston or New York City are more likely to see a small scale atmospheric chemistry flights than Lagos, even though Lagos has worse and more complex air pollution than either of those cities. FLUXNET, the global network of eddy covariance towers, does not have a single eddy covariance tower in Nigeria (*U.S.D.O.E*, 2020). It would be to the benefit of the global Earth science community if more data was gathered in understudied places. It would be good for some of that science to come from local research, and it could be beneficial if non-African research resources

were invested in a proper way into growing local research capacity. This is not dissimilar to the notion that it is proper for wealthy countries to help poorer ones in efforts such as mitigating CFC's.

ATom did not measure HONO, which is a key tracer of the process proposed by *Wang et al.* (2020). A future air campaign investigating heterogeneous N₂O formation could focus on a single city and carry instruments to measure reactive nitrogen species, SO₂, sulfur PM, and HONO. There are many small scale urban N₂O emission processes that could also be observed by such a mission. In general, the ATom trajectory style of background modeling is well suited to local or regional air campaign data. Our clustering method applied with chemical data could also be amenable to a local redox chemistry focused flight campaign.

The discussion of heterogeneous N₂O formation is also relevant to air quality. *Wang et al.* (2020)'s investigation was motivated by the of Beijing winter haze, and the negative health effects of high PM concentrations. Lagos is known to have a severe air pollution problem as well. Targeting the broader problem of atmospheric sulfur–nitrogen redox chemistry has positive outcomes for greenhouse gasses and ozone depleting substances beyond the known benefits to PM pollution and acid rain.

We have painted a picture of a strong urban biomass burning N₂O source in the African outflow. We connected that source to current understanding of N₂O emissions, and investigated a potential unaccounted for chemical N₂O source. These efforts to better understand a regional atmospheric chemistry problem are connected to bigger questions, both through the need to consider global atmospheric transport, and through their relevance to the climate and humanity's place within the Earth system.

"Stratospheric traces of our transitory flight
Trails of condensation held
in narrow bands of white

...

Horizon to Horizon
memory written in the wind

...

Atmospheric phases make the transitory last

...

In a vapor trail"

– Neil Peart, *Vapor Trails*

Appendix A

Appendix

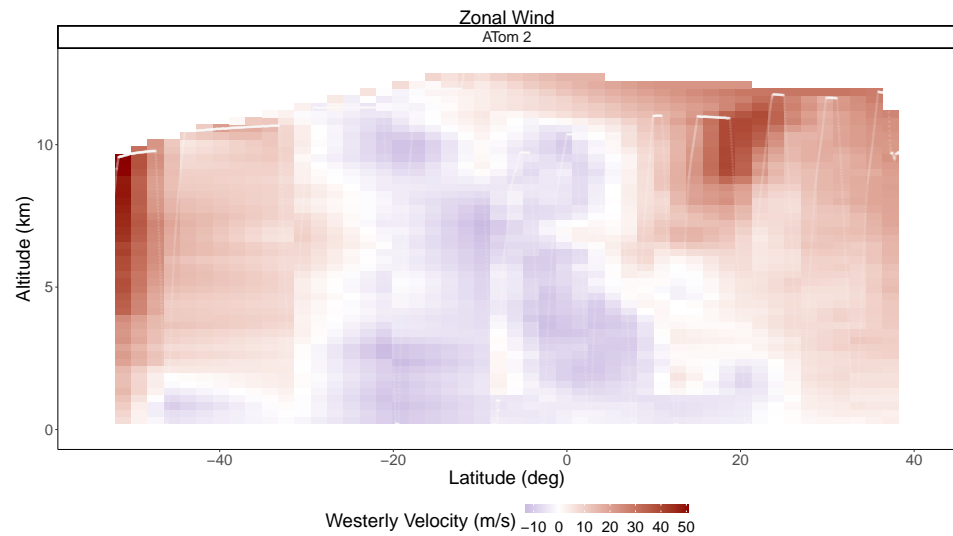


Figure A.1: Transect of ATom observed zonal wind. The key feature is the strong Easterlies centered on the Equator

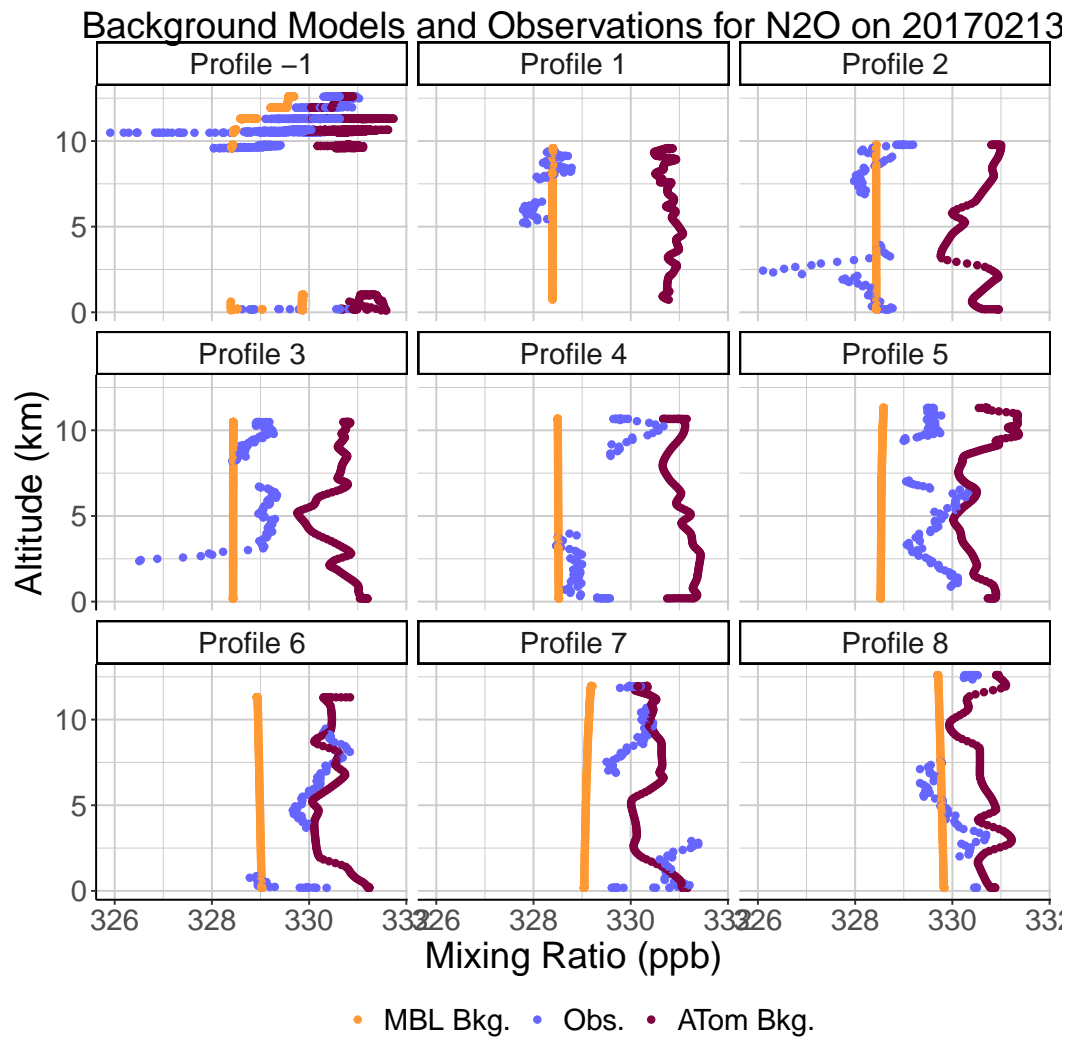


Figure A.2

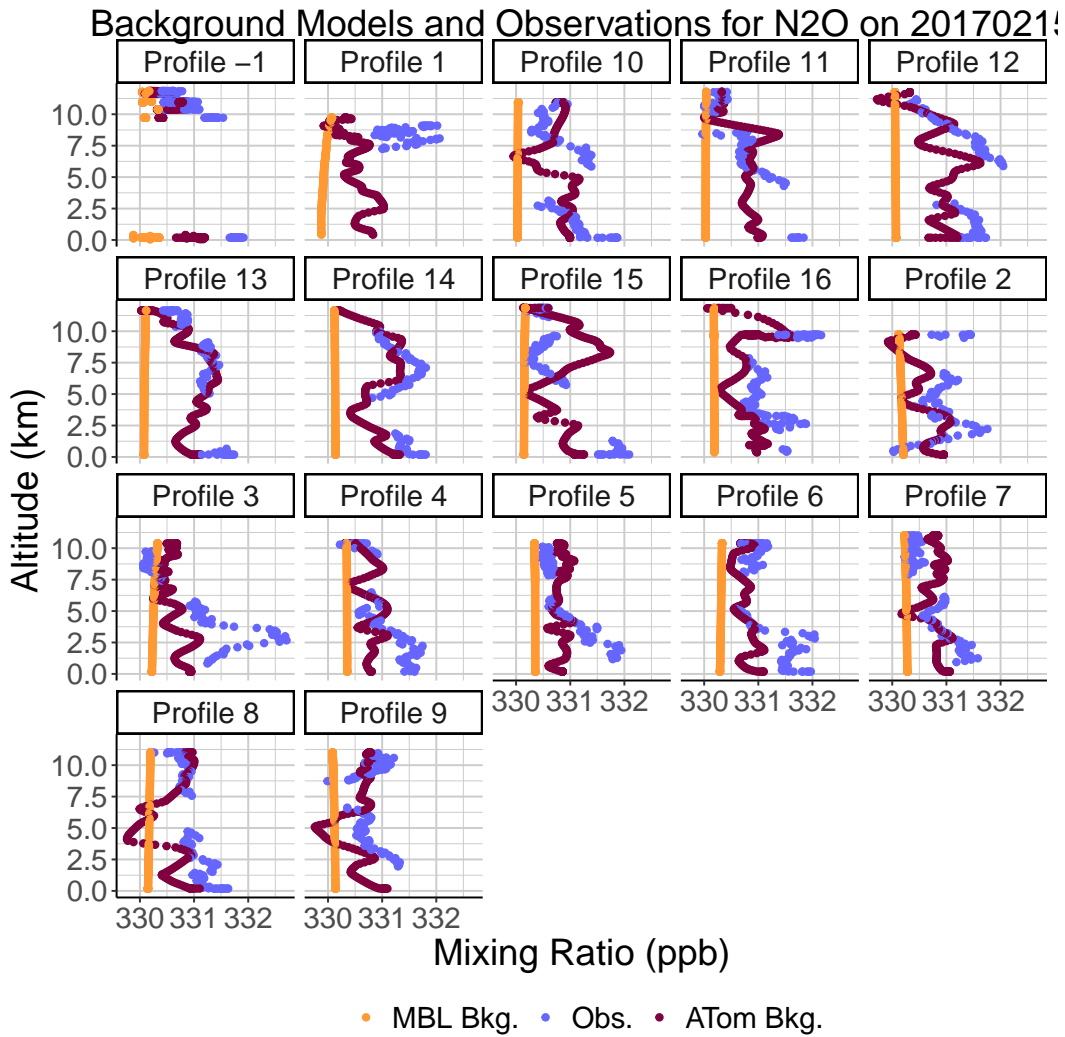


Figure A.3

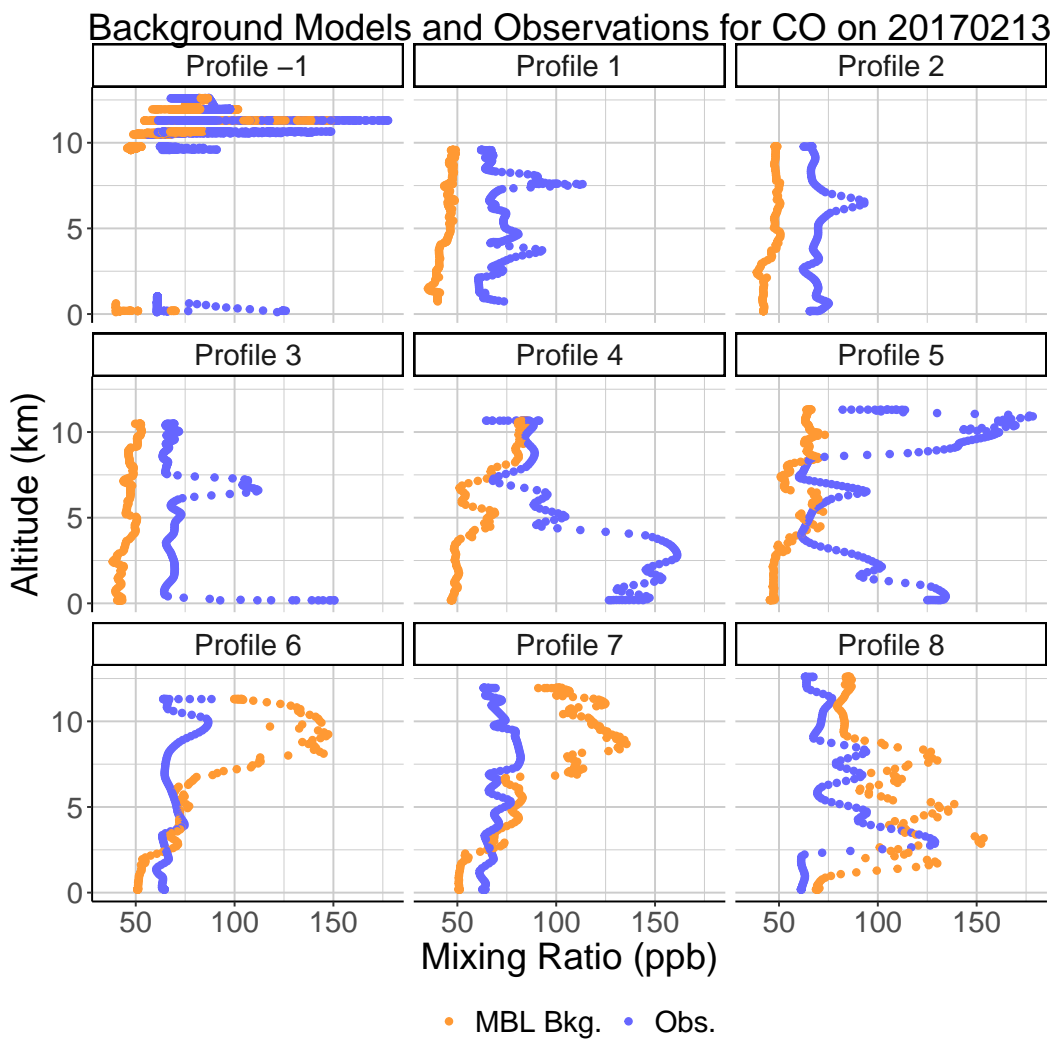


Figure A.4

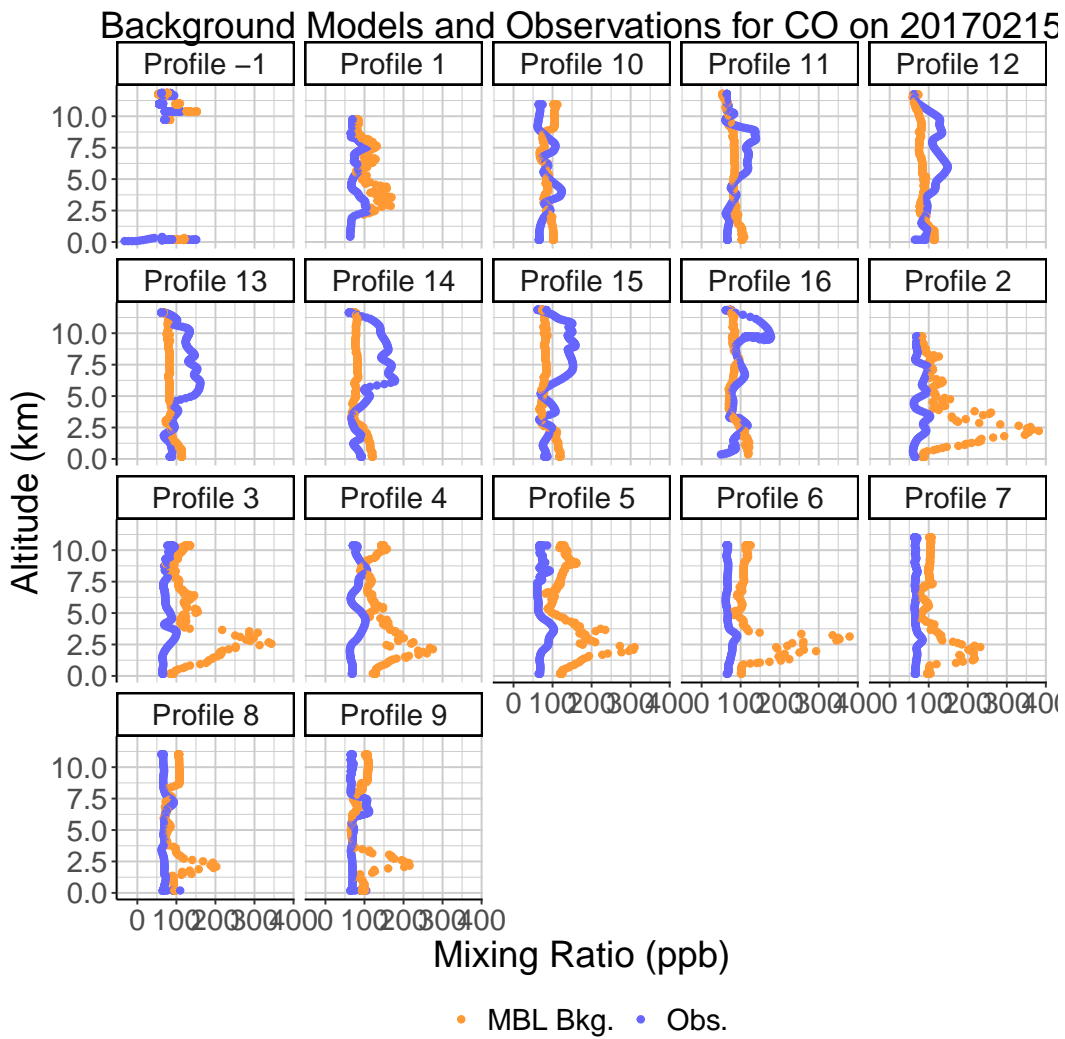


Figure A.5

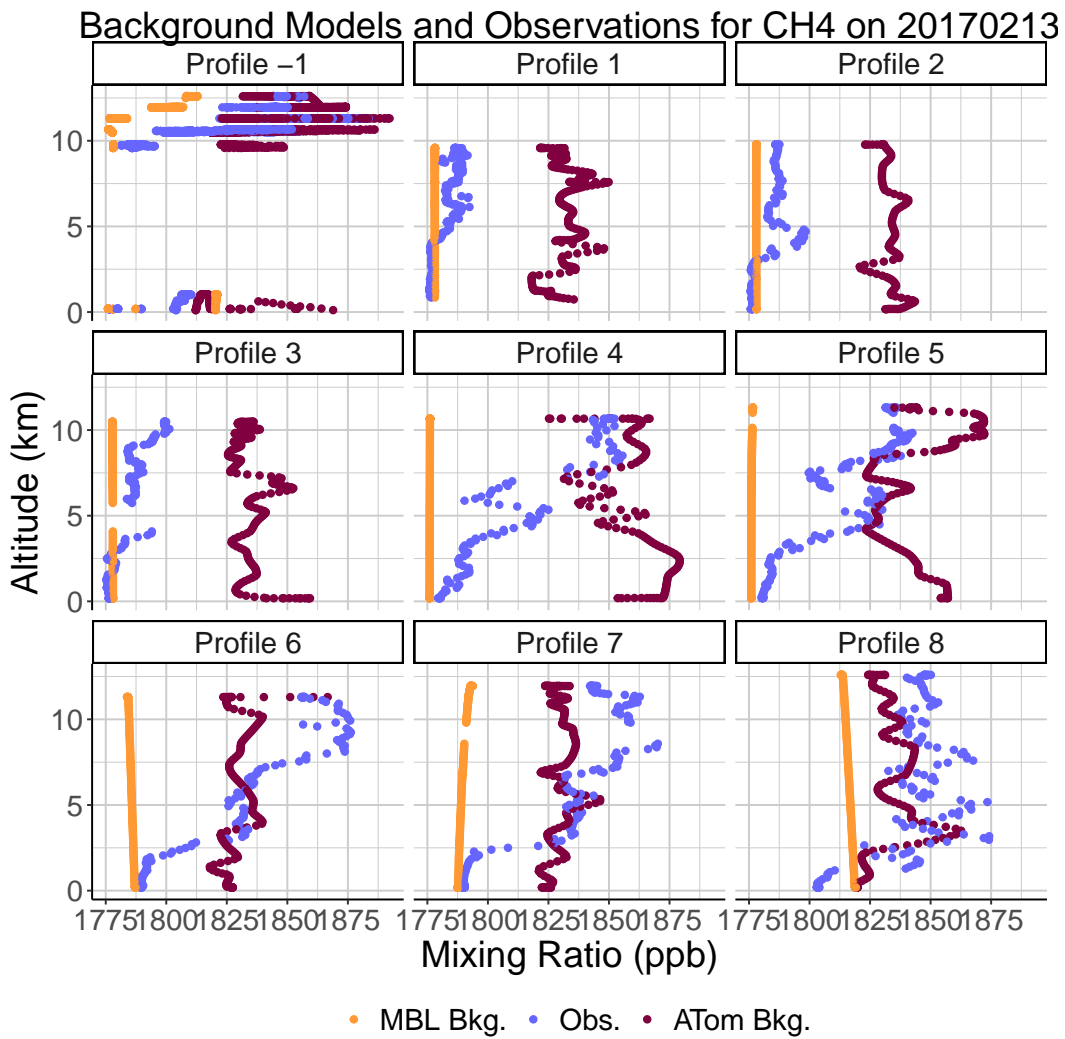


Figure A.6

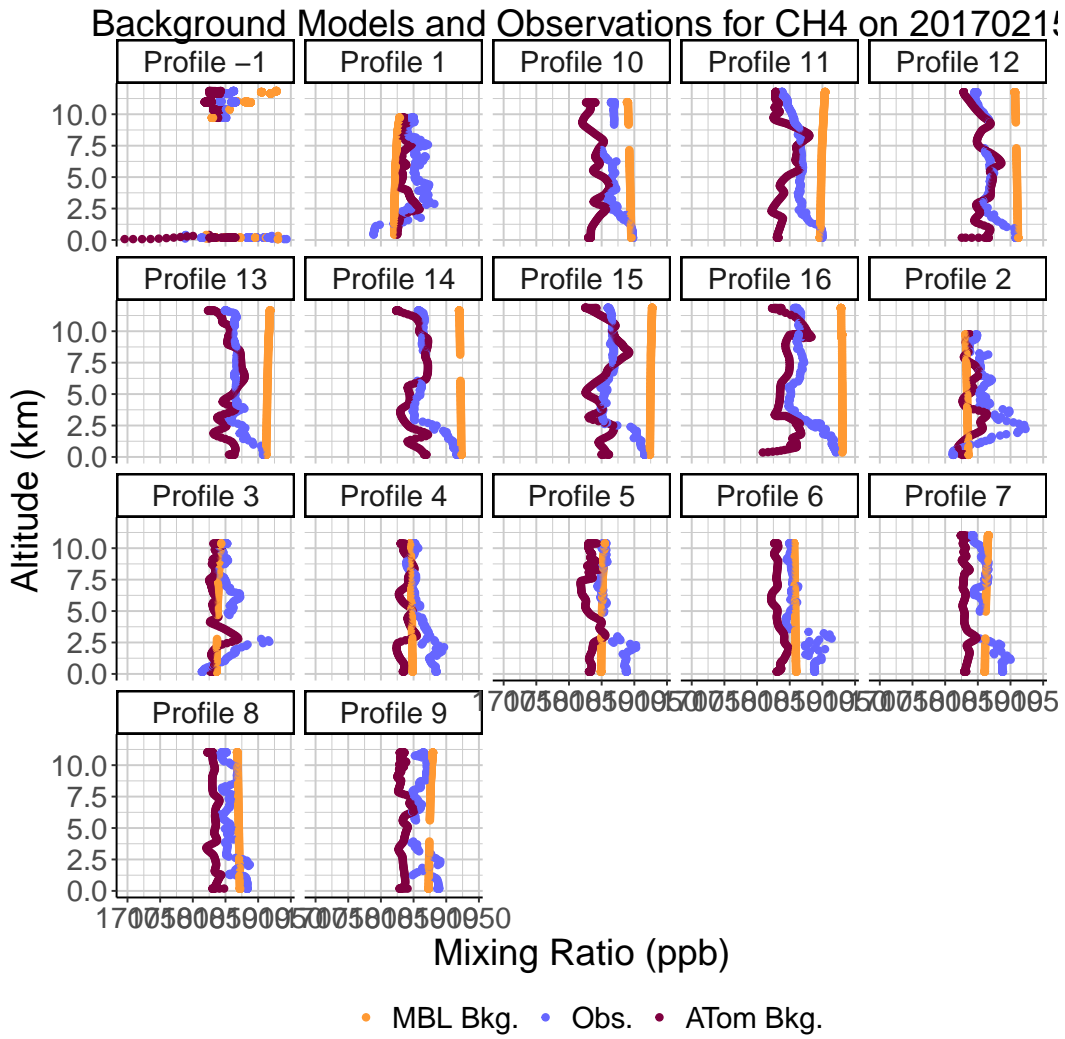


Figure A.7

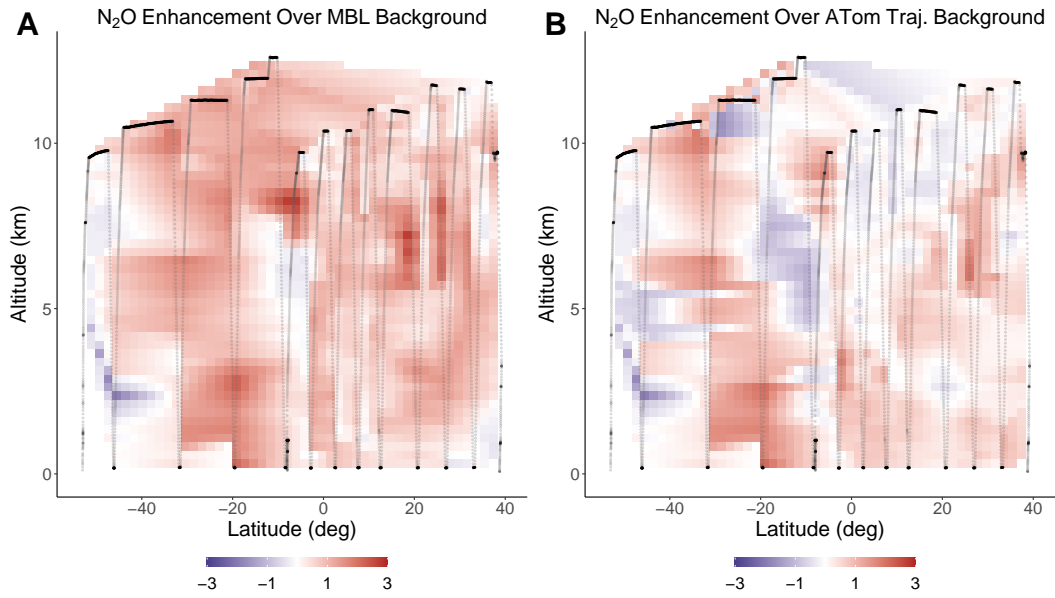


Figure A.8: Transect of MBL (A) and ATom trajectory (B) modeled background calculated N_2O enhancement for ATom 2

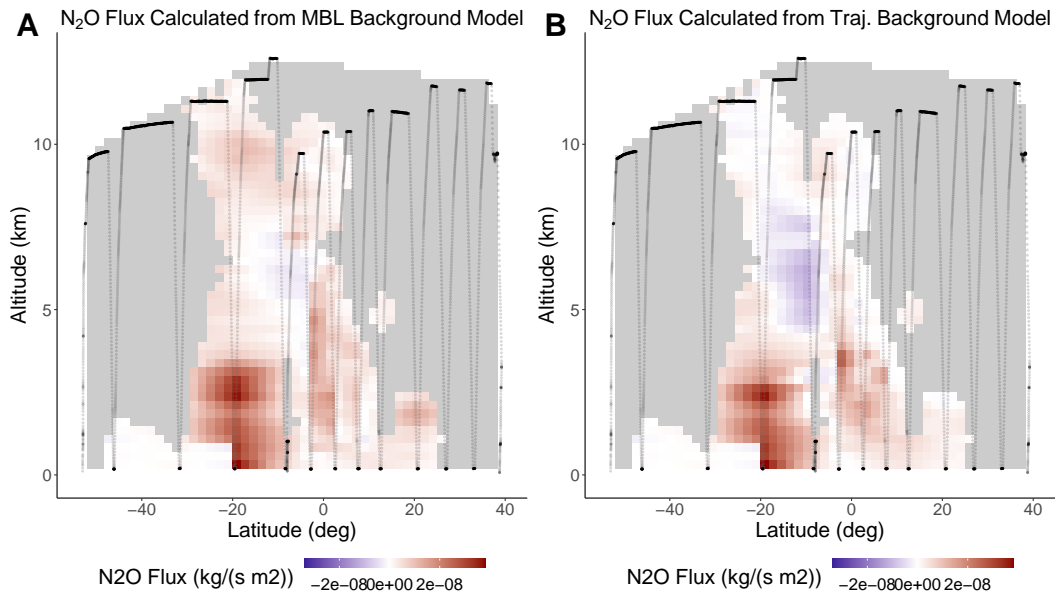


Figure A.9: Transect of MBL (A) and ATom trajectory (B) modeled background calculated N_2O flux, restricted to positive Easterly zonal wind for ATom 2

ATom 2: Average Footprints of Footprint Derived Clusters

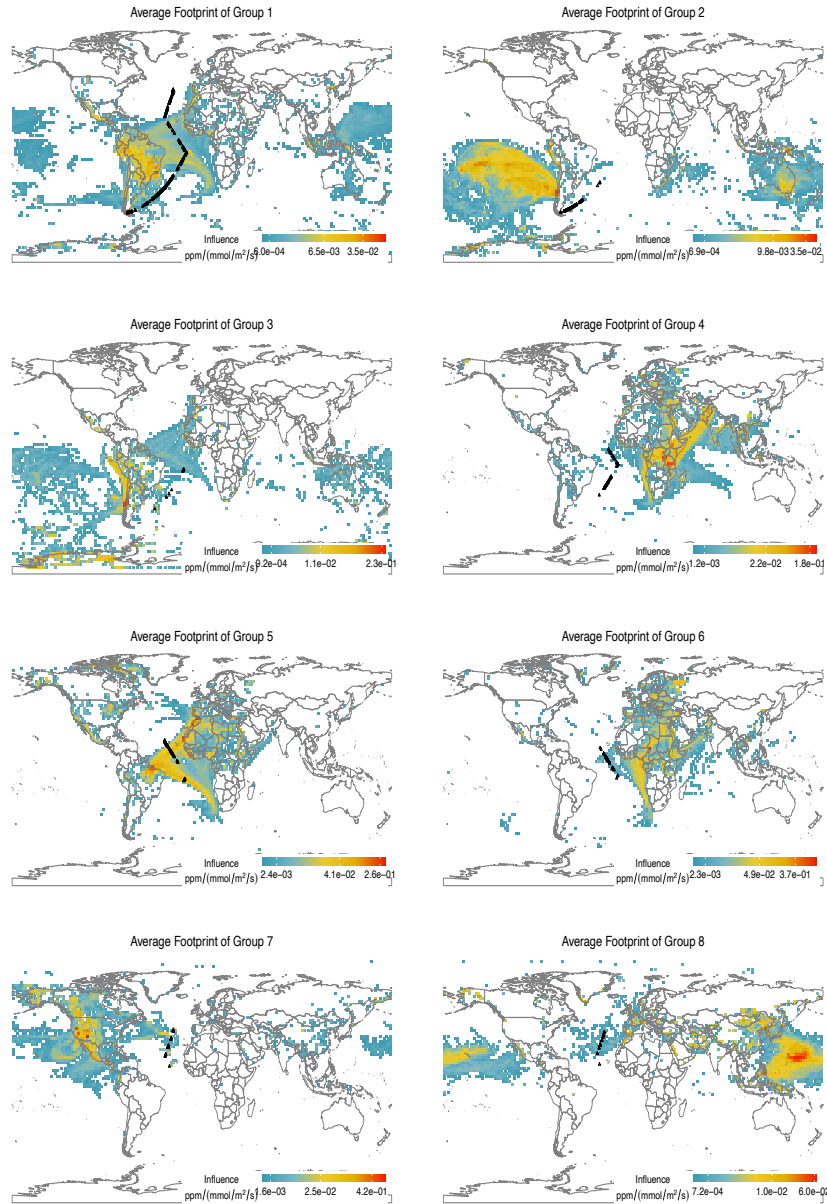


Figure A.10: Average Footprints of ATom 2 Clusters
58

ATom 3: Average Footprints of Footprint Derived Clusters

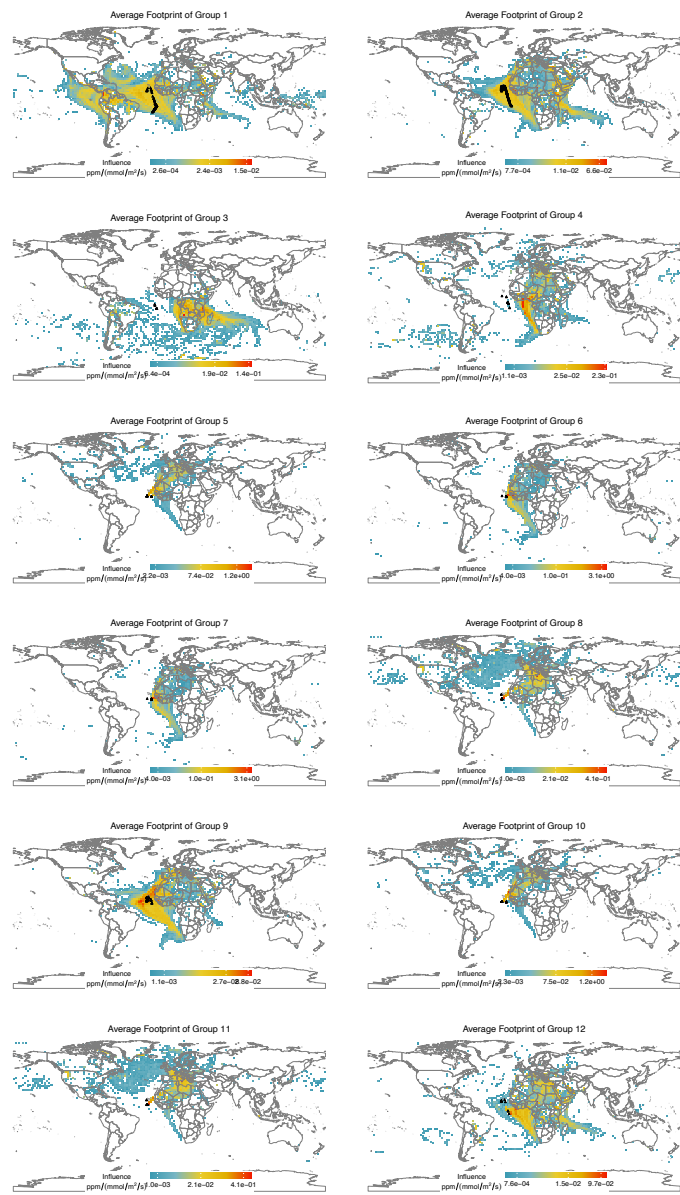


Figure A.11: Average Footprints of ATom 3 Clusters

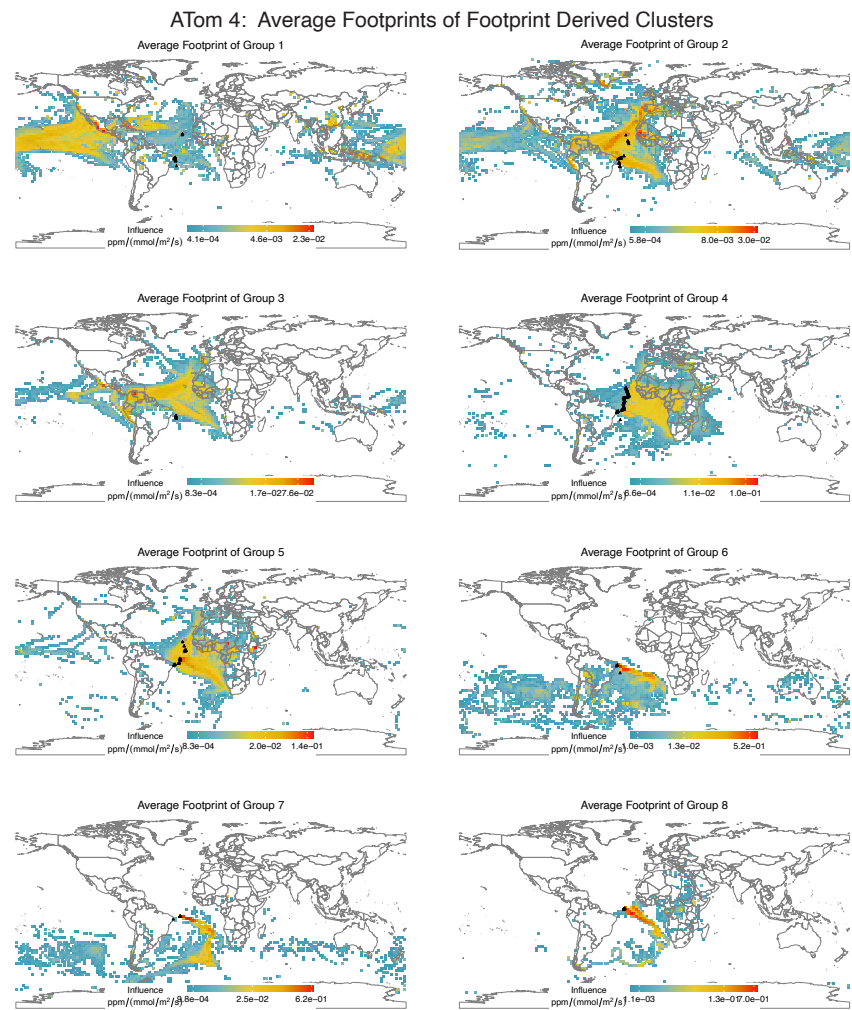


Figure A.12: Average Footprints of ATom 4 Clusters

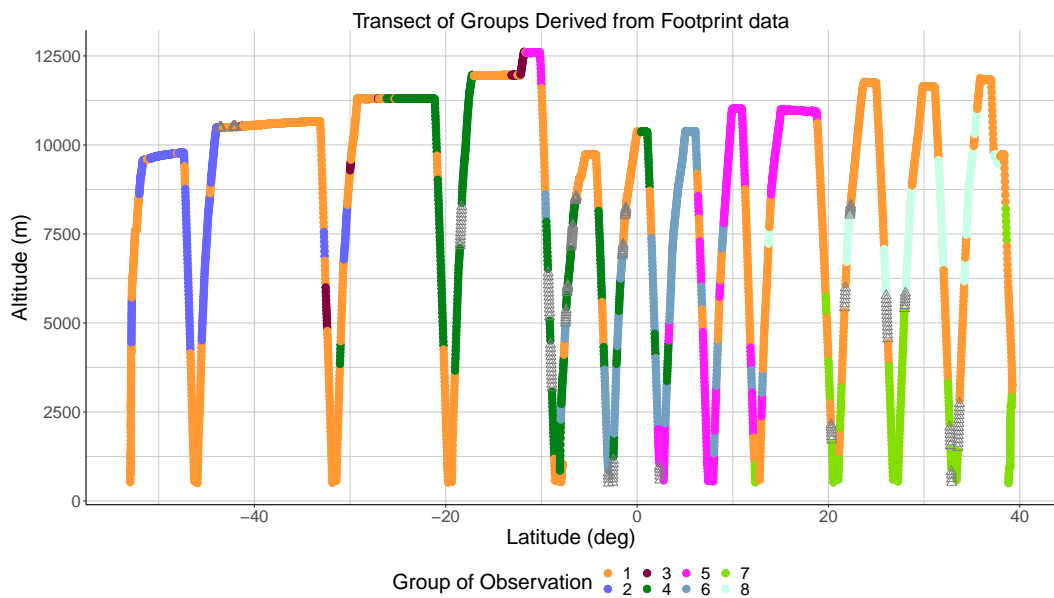


Figure A.13: Transect of ATom 2 Clusters.

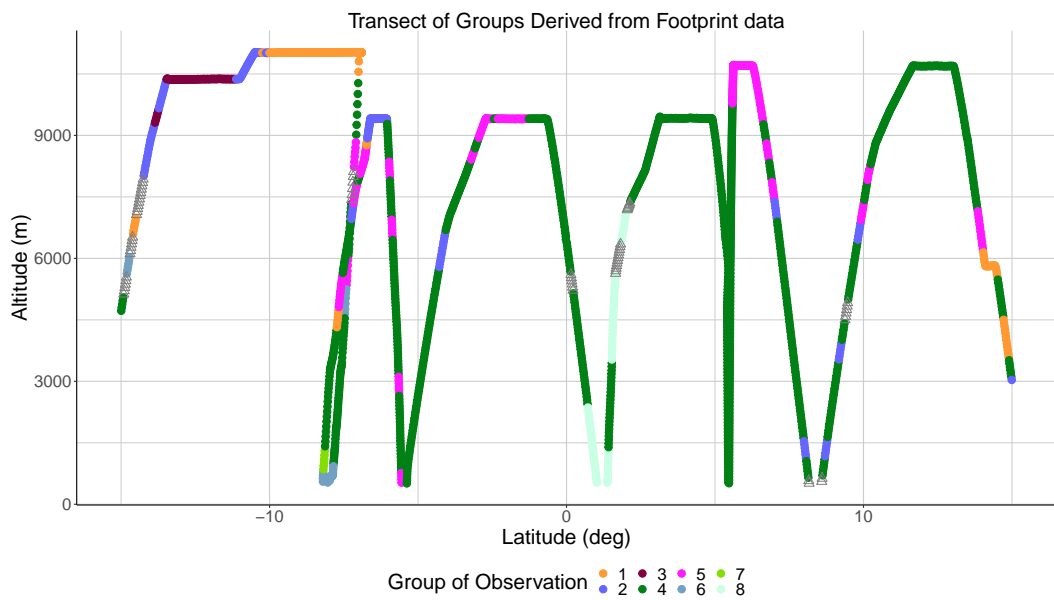


Figure A.14: Transect of ATom 4 Clusters

References

- Akima, H. (1991), A method of univariate interpolation that has the accuracy of a third-degree polynomial, *ACM Transactions on Mathematical Software*, 17(3), 341–366, doi:10.1145/114697.116810.
- Akima, H. (1996), Algorithm 761: Scattered-data surface fitting that has the accuracy of a cubic polynomial, *ACM Transactions on Mathematical Software*, 22(3), 362–371, doi:10.1145/232826.232856.
- Anderson, J. G., D. W. Toohey, and W. H. Brune (1991), Free Radicals within the Antarctic Vortex: The Role of CFCs in Antarctic Ozone Loss, *Science*, 251(4989), 39, num Pages: 8 Place: Washington, United States Publisher: The American Association for the Advancement of Science.
- Bowman, K. P. (1993), Large-scale isentropic mixing properties of the Antarctic polar vortex from analyzed winds, *Journal of Geophysical Research*, 98(D12), 23,013, doi:10.1029/93JD02599.
- Box, G. E. P., and N. R. Draper (1987), *Empirical model-building and response surfaces*, Wiley series in probability and mathematical statistics, Wiley, New York.
- Butterbach-Bahl, K., E. M. Baggs, M. Dannenmann, R. Kiese, and S. Zechmeister-Boltenstern (2013), Nitrous oxide emissions from soils: how well do we understand the processes and their controls?, *Philosophical Transactions of the Royal Society B: Biological Sciences*, 368(1621), 20130,122, doi:10.1098/rstb.2013.0122.
- Ciais, P., G. B. Bopp, L., V. Brovkin, J. Canadell, A. Chhabra, R. DeFries, J. Galloway, M. Heimann, C. Jones, C. L. Quéré, R. Myneni, S. Piao, P. Thornton, and C. Sabine (2013), Carbon and Other Biogeochemical Cycles, in *Climate Change 2013: The Physical Science Basis. Contribution of Working Group I to the Fifth Assessment Report of the Intergovernmental Panel on Climate Change*, Cambridge University Press, Cambridge, United Kingdom and New York, NY USA.

Craney, T. A., and J. G. Surles (2002), Model-Dependent Variance Inflation Factor Cutoff Values, *Quality Engineering*, 14(3), 391–403, doi:10.1081/QEN-120001878, publisher: Taylor & Francis Ltd.

Crutzen, P. J., and M. O. Andreae (1990), Biomass Burning in the Tropics: Impact on Atmospheric Chemistry and Biogeochemical Cycles, *Science; Washington*, 250(4988), 1669.

Crutzen, P. J., L. E. Heidt, J. P. Krasnec, W. H. Pollock, and W. Seiler (1979), Biomass burning as a source of atmospheric gases CO, H₂, N₂O, NO, CH₃Cl and COS, *Nature*, 282(5736), 253–256, doi:10.1038/282253a0, number: 5736 Publisher: Nature Publishing Group.

Dangal, S. R. S., H. Tian, R. Xu, J. Chang, J. G. Canadell, P. Ciais, S. Pan, J. Yang, and B. Zhang (2019), Global Nitrous Oxide Emissions From Pasturelands and Rangelands: Magnitude, Spatiotemporal Patterns, and Attribution, *Global Biogeochemical Cycles*, 33(2), 200–222, doi:10.1029/2018GB006091, _eprint: <https://onlinelibrary.wiley.com/doi/pdf/10.1029/2018GB006091>.

der Werf, G. R. v., J. T. Randerson, L. Giglio, G. J. Collatz, M. Mu, P. S. Kasischke, D. C. Morton, R. S. DeFries, Y. Jin, and T. T. van Leeuwen (2010), Global fire emissions and the contribution of deforestation, savanna, forest, agricultural, and peat fires (1997–2009), *Atmospheric Chemistry and Physics*, 10(23), 11,707, num Pages: 11707 Place: Katlenburg-Lindau, Germany Publisher: Copernicus GmbH.

Donev, J., K. Stenhouse, and J. Jenden (2019), Coal fired power plant - Energy Education.

Efron, B. (1979), Bootstrap Methods: Another Look at the Jackknife, *The Annals of Statistics*, 7(1), 1–26, publisher: Institute of Mathematical Statistics.

Ester, M., H.-P. Kriegel, J. Sander, and X. Xu (1996), A density-based algorithm for discovering clusters in large spatial databases with noise., in *Kdd*, vol. 96, pp. 226–231, issue: 34.

Forster, G., R. C. Upstill-Goddard, N. Gist, C. Robinson, G. Uher, and E. M. S. Woodward (2009), Nitrous oxide and methane in the Atlantic Ocean between 50N and 52S: Latitudinal distribution and sea-to-air flux,

Deep Sea Research Part II: Topical Studies in Oceanography, 56(15), 964–976, doi:10.1016/j.dsr2.2008.12.002.

Fox, J., and G. Monette (1992), Generalized Collinearity Diagnostics, *Journal of the American Statistical Association*, 87(417), 178–183, doi:10.1080/01621459.1992.10475190.

Galloway, J. N., J. D. Aber, J. W. Erisman, S. P. Seitzinger, and e. al (2003), The nitrogen cascade, *Bioscience*, 53(4), 341–356, doi: [http://dx.doi.org.ezp-prod1.hul.harvard.edu/10.1641/0006-3568\(2003\)053\[0341:TNC\]2.0.CO;2](http://dx.doi.org.ezp-prod1.hul.harvard.edu/10.1641/0006-3568(2003)053[0341:TNC]2.0.CO;2), num Pages: 341-356 Place: Oxford, United Kingdom Publisher: Oxford University Press Section: Articles.

Giglio, L., and C. Justice (2015), MOD14A2 MODIS/Terra Thermal Anomalies/Fire 8-Day L3 Global 1km SIN Grid V006, doi:10.5067/MODIS/MOD14A2.006, type: dataset.

Gonzalez, Y., R. Commane, E. Manninen, B. C. Daube, L. Schiferl, J. B. McManus, K. McKain, E. J. Hintsa, J. W. Elkins, S. A. Montzka, C. Sweeney, F. Moore, J. L. Jimenez, P. Campuzano Jost, T. B. Ryerson, I. Bourgeois, J. Peischl, C. R. Thompson, E. Ray, P. O. Wennberg, J. Crounse, M. Kim, H. M. Allen, P. Newman, B. B. Stephens, E. C. Apel, R. S. Hornbrook, B. A. Nault, E. Morgan, and S. C. Wofsy (2021), Impact of stratospheric air and surface emissions on tropospheric nitrous oxide during ATom, *preprint*, Gases/Field Measurements/Troposphere/Chemistry (chemical composition and reactions), doi:10.5194/acp-2021-167.

Gvakharia, A., E. A. Kort, M. L. Smith, and S. Conley (2020), Evaluating Cropland N₂O Emissions and Fertilizer Plant Greenhouse Gas Emissions With Airborne Observations, *Journal of Geophysical Research: Atmospheres*, 125(16), doi:10.1029/2020JD032815.

Legendre, A. M. (1806), *Nouvelles méthodes pour la détermination des orbites des comètes, avec un supplément contenant divers perfectionnemens de ces méthodes et leur application aux deux comètes de 1805*, Courcier, Paris.

Lin, J. C., C. Gerbig, S. C. Wofsy, A. E. Andrews, B. C. Daube, K. J. Davis, and C. A. Grainger (2003), A near-field tool for simulating the upstream

influence of atmospheric observations: The Stochastic Time-Inverted Lagrangian Transport (STILT) model, *Journal of Geophysical Research: Atmospheres*, 108(D16), n/a–n/a, doi:10.1029/2002JD003161.

Lueker, T. J., S. J. Walker, M. K. Vollmer, R. F. Keeling, C. D. Nevison, R. F. Weiss, and H. E. Garcia (2003), Coastal upwelling air-sea fluxes revealed in atmospheric observations of O₂/N₂, CO₂ and N₂O, *Geophysical Research Letters*, 30(6), doi:<https://doi.org/10.1029/2002GL016615>, eprint: <https://onlinelibrary.wiley.com/doi/pdf/10.1029/2002GL016615>.

Marais, E., D. Jacob, K. Wecht, C. Lerot, L. Zhang, K. Yu, T. Kurosu, K. Chance, and B. Sauvage (2014), Anthropogenic emissions in Nigeria and implications for atmospheric ozone pollution: A view from space, *Atmospheric Environment*, 99, 32–40, doi:10.1016/j.atmosenv.2014.09.055.

Marais, E. A., and C. Wiedinmyer (2016), Air Quality Impact of Diffuse and Inefficient Combustion Emissions in Africa (DICE-Africa), *Environmental Science & Technology*, 50(19), 10,739–10,745, doi:10.1021/acs.est.6b02602, publisher: American Chemical Society.

Martin, L., D. E. Damschen, and H. S. Judeikis (1981), The reactions of nitrogen oxides with SO₂ in aqueous aerosols, *Atmospheric Environment* (1967), 15(2), 191–195, doi:10.1016/0004-6981(81)90010-X.

Meure, C. M., D. Etheridge, C. Trudinger, P. Steele, R. Langenfelds, T. v. Ommen, A. Smith, and J. Elkins (2006), Law Dome CO₂, CH₄ and N₂O ice core records extended to 2000 years BP, *Geophysical Research Letters*, 33(14), doi:<https://doi.org/10.1029/2006GL026152>, eprint: <https://onlinelibrary.wiley.com/doi/pdf/10.1029/2006GL026152>.

Molina, M. J., and F. S. Rowland (1974), Stratospheric sink for chlorofluoromethanes: chlorine atom-catalysed destruction of ozone, *Nature*, 249(5460), 810–812, doi:10.1038/249810a0, number: 5460 Publisher: Nature Publishing Group.

Molod, A., L. Takacs, M. Suarez, and J. Bacmeister (2015), Development of the GEOS-5 atmospheric general circulation model: evolution from MERRA to MERRA2, *Geoscientific Model Development*, 8(5), 1339–1356, doi:10.5194/gmd-8-1339-2015.

Naqvi, S. W. A., D. A. Jayakumar, P. V. Narvekar, H. Nalk, and e. al (2000), Increased marine production of N₂O due to intensifying anoxia on the Indian continental shelf, *Nature*, 408(6810), 346–9, doi:<http://dx.doi.org.ezp-prod1.hul.harvard.edu/10.1038/35042551>, num Pages: 346-9 Place: London, United States Publisher: Nature Publishing Group.

NCEP (2019), Global Forecast System.

Nevison, C. D., T. J. Lueker, and R. F. Weiss (2004), Quantifying the nitrous oxide source from coastal upwelling, *Global Biogeochemical Cycles*, 18(1), n/a–n/a, doi:[10.1029/2003GB002110](https://doi.org/10.1029/2003GB002110).

Nevison, C. D., E. Dlugokencky, G. Dutton, J. W. Elkins, P. Fraser, B. Hall, P. B. Krummel, R. L. Langenfelds, S. O'Doherty, R. G. Prinn, L. P. Steele, and R. F. Weiss (2011), Exploring causes of interannual variability in the seasonal cycles of tropospheric nitrous oxide, *Atmospheric Chemistry and Physics; Katlenburg-Lindau*, 11(8), 3713, num Pages: 3713 Place: Katlenburg-Lindau, Germany, Katlenburg-Lindau Publisher: Copernicus GmbH.

Olivier, J. G. J., A. F. Bouwman, C. W. M. van der Maas, and J. J. M. Berdowski (1994), Emission database for global atmospheric research (Edgar), *Environmental Monitoring and Assessment*, 31(1), 93–106, doi: [10.1007/BF00547184](https://doi.org/10.1007/BF00547184).

Pires, M. (1996), The Heterogeneous Formation of N₂O over Bulk Condensed Phases in the Presence of SO₂ at High Humidities, *Journal of Atmospheric Chemistry*, p. 22.

Pires, M. A., and M. J. Rossi (1997), The heterogeneous formation of N₂O in the presence of acidic solutions: Experiments and modeling, *International Journal of Chemical Kinetics*, p. 24.

Prather, M. J., J. Hsu, N. M. DeLuca, C. H. Jackman, L. D. Oman, A. R. Douglass, E. L. Fleming, S. E. Strahan, S. D. Steenrod, O. A. Søvde, I. S. A. Isaksen, L. Froidevaux, and B. Funke (2015), Measuring and modeling the lifetime of nitrous oxide including its variability, *Journal of Geophysical Research: Atmospheres*, 120(11), 5693–5705, doi:[10.1002/2015JD023267](https://doi.org/10.1002/2015JD023267), eprint: <https://onlinelibrary.wiley.com/doi/pdf/10.1002/2015JD023267>.

R Core Team (2020), R: A Language and Environment for Statistical Computing.

Randerson, J. T., G. Van der Werf, L. Giglio, G. Collatz, and P. Kasibhatla (2017), Global Fire Emissions Database, Version 4.1 (GFEDv4), doi:10.3334/ORNLDAAAC/1293, publisher: ORNL Distributed Active Archive Center.

Ravishankara, A. R., J. S. Daniel, and R. W. Portmann (2009), Nitrous Oxide (N₂O): The Dominant Ozone-Depleting Substance Emitted in the 21st Century, *Science*, 326(5949), 123–125, doi:10.1126/science.1176985, publisher: American Association for the Advancement of Science Section: Report.

Sakamoto, Y., M. Ishiguro, and G. Kitagawa (1986), *Akaike information criterion statistics*, Mathematics and its applications (Japanese series), KTK Scientific Publishers ; D. Reidel ; Sold and distributed in the U.S.A. and Canada by Kluwer Academic Publishers, Tokyo : Dordrecht ; Boston : Hingham, MA.

Santoro, A. E., C. Buchwald, M. R. McIlvin, and K. L. Casciotti (2011), Isotopic Signature of N₂O Produced by Marine Ammonia-Oxidizing Archaea, *Science*, 333(6047), 1282–1285, doi:10.1126/science.1208239.

Schill, G. P., K. D. Froyd, H. Bian, A. Kupc, C. Williamson, C. A. Brock, E. Ray, R. S. Hornbrook, A. J. Hills, E. C. Apel, M. Chin, P. R. Colarco, and D. M. Murphy (2020), Widespread biomass burning smoke throughout the remote troposphere, *Nature Geoscience*, 13(6), 422–427, doi:10.1038/s41561-020-0586-1.

Stein, A. F., R. R. Draxler, G. D. Rolph, B. J. B. Stunder, M. D. Cohen, and F. Ngan (2015), NOAA's HYSPLIT Atmospheric Transport and Dispersion Modeling System, *Bulletin of the American Meteorological Society*, 96(12), 2059–2077, doi:10.1175/BAMS-D-14-00110.1.

Stephens, B. B., R. F. Keeling, M. Heimann, K. D. Six, R. Murnane, and K. Caldeira (1998), Testing global ocean carbon cycle models using measurements of atmospheric O₂ and CO₂ concentration, *Global Biogeochemical Cycles*, 12(2), 213–230, doi:<https://doi.org/10.1029/97GB03500>, eprint: <https://onlinelibrary.wiley.com/doi/pdf/10.1029/97GB03500>.

Thompson, R. L., P. K. Patra, K. Ishijima, E. Saikawa, M. Corazza, U. Karstens, C. Wilson, C. Bergamaschi, E. Dlugokencky, C. Sweeney, R. G. Prinn, R. F. Weiss, S. O'Doherty, P. J. Fraser, L. P. Steele, P. B. Krummel, M. Saunois, M. Chipperfield, and P. Bousquet (2014), TransCom N₂O model inter-comparison – Part 1: Assessing the influence of transport and surface fluxes on tropospheric N₂O variability, 4349–4368, doi: 10.5194/acp-14-4349-2014, accepted: 2015-02-12T14:00:46Z.

Thompson, R. L., L. Lassaletta, P. K. Patra, C. Wilson, K. C. Wells, A. Gressent, E. N. Koffi, M. P. Chipperfield, W. Winiwarter, E. A. Davidson, H. Tian, and J. G. Canadell (2019), Acceleration of global N₂O emissions seen from two decades of atmospheric inversion, *Nature Climate Change*, 9(12), 993–998, doi:10.1038/s41558-019-0613-7, number: 12 Publisher: Nature Publishing Group.

Tian, H., J. Yang, R. Xu, C. Lu, J. G. Canadell, E. A. Davidson, R. B. Jackson, A. Arneth, J. Chang, P. Ciais, S. Gerber, A. Ito, F. Joos, S. Lienert, P. Messina, S. Olin, S. Pan, C. Peng, E. Saikawa, R. L. Thompson, N. Vuichard, W. Winiwarter, S. Zaehle, and B. Zhang (2019), Global soil nitrous oxide emissions since the preindustrial era estimated by an ensemble of terrestrial biosphere models: Magnitude, attribution, and uncertainty, *Global Change Biology*, 25(2), 640–659, doi:10.1111/gcb.14514.

Tian, H., R. Xu, J. G. Canadell, R. L. Thompson, W. Winiwarter, P. Suntharalingam, E. A. Davidson, P. Ciais, R. B. Jackson, G. Janssens-Maenhout, M. J. Prather, P. Regnier, N. Pan, S. Pan, G. P. Peters, H. Shi, F. N. Tubiello, S. Zaehle, F. Zhou, A. Arneth, G. Battaglia, S. Berthet, L. Bopp, A. F. Bouwman, E. T. Buitenhuis, J. Chang, M. P. Chipperfield, S. R. S. Dangal, E. Dlugokencky, J. W. Elkins, B. D. Eyre, B. Fu, B. Hall, A. Ito, F. Joos, P. B. Krummel, A. Landolfi, G. G. Laruelle, R. Lauerwald, W. Li, S. Lienert, T. Maavara, M. MacLeod, D. B. Millet, S. Olin, P. K. Patra, R. G. Prinn, P. A. Raymond, D. J. Ruiz, G. R. van der Werf, N. Vuichard, J. Wang, R. F. Weiss, K. C. Wells, C. Wilson, J. Yang, and Y. Yao (2020), A comprehensive quantification of global nitrous oxide sources and sinks, *Nature*, 586(7828), 248–256, doi:10.1038/s41586-020-2780-0.

U.S.D.O.E (2020), FLUXNET - The Data Portal serving the FLUXNET community.

U.S.EIA (2020), Coal explained - U.S. Energy Information Administration (EIA).

Van der Maaten, L., and G. Hinton (2008), Visualizing data using t-SNE., *Journal of machine learning research*, 9(11).

Wang, J., J. Li, J. Ye, J. Zhao, Y. Wu, J. Hu, D. Liu, D. Nie, F. Shen, X. Huang, D. D. Huang, D. Ji, X. Sun, W. Xu, J. Guo, S. Song, Y. Qin, P. Liu, J. R. Turner, H. C. Lee, S. Hwang, H. Liao, S. T. Martin, Q. Zhang, M. Chen, Y. Sun, X. Ge, and D. J. Jacob (2020), Fast sulfate formation from oxidation of SO₂ by NO₂ and HONO observed in Beijing haze, *Nature Communications*, 11(1), 2844, doi:10.1038/s41467-020-16683-x.

Waugh, D. W., A. M. Crotwell, E. J. Dlugokencky, G. S. Dutton, J. W. Elkins, B. D. Hall, E. J. Hintsa, D. F. Hurst, S. A. Montzka, D. J. Mondeel, F. L. Moore, J. D. Nance, E. A. Ray, S. D. Steenrod, S. E. Strahan, and C. Sweeney (2013), Tropospheric SF₆ : Age of air from the Northern Hemisphere midlatitude surface: SF₆ AND AGE OF TROPOSPHERIC AIR, *Journal of Geophysical Research: Atmospheres*, 118(19), 11,429–11,441, doi:10.1002/jgrd.50848.

Wilkes, W., and B. Parkin (2020), New German Coal Plant Could Threaten Merkel's Final Climate Push, *Bloomberg.com*.

Wofsy, S. C., S. Afshar, H. M. Allen, E. C. Apel, E. C. Asher, B. Barletta, J. Bent, H. Bian, B. C. Biggs, D. R. Blake, N. Blake, I. Bourgeois, C. A. Brock, W. H. Brune, J. W. Budney, T. P. Bui, A. Butler, P. Campuzano-Jost, C. S. Chang, M. Chin, R. Commane, G. Correa, J. D. Crounse, P. D. Cullis, B. C. Daube, D. A. Day, J. M. Dean-Day, J. E. Dibb, J. P. Digangi, G. S. Diskin, M. Dollner, J. W. Elkins, F. Erdesz, A. M. Fiore, C. M. Flynn, K. D. Froyd, D. W. Gesler, S. R. Hall, T. F. Hanisco, R. A. Hannun, A. J. Hills, E. J. Hintsa, A. Hoffman, R. S. Hornbrook, L. G. Huey, S. Hughes, J. L. Jimenez, B. J. Johnson, J. M. Katich, R. F. Keeling, M. J. Kim, A. Kupc, L. R. Lait, J.-F. Lamarque, J. Liu, K. Mckain, R. J. McLaughlin, S. Meinardi, D. O. Miller, S. A. Montzka, F. L. Moore, E. J. Morgan, D. M. Murphy, L. T. Murray, B. A. Nault, J. A. Neuman, P. A. Newman, J. M. Nicely, X. Pan, W. Paplawsky, J. Peischl, M. J. Prather, D. J. Price, E. A. Ray, J. M. Reeves, M. Richardson, A. W. Rollins, K. H. Rosenlof, T. B. Ryerson, E. Scheuer,

G. P. Schill, J. C. Schroder, J. P. Schwarz, J. M. St. Clair, S. D. Steenrod, B. B. Stephens, S. A. Strode, C. Sweeney, D. Tanner, A. P. Teng, A. B. Thames, C. R. Thompson, K. Ullmann, P. R. Veres, N. Vizenor, N. L. Wagner, A. Watt, R. Weber, B. B. Weinzierl, P. O. Wennberg, C. J. Williamson, J. C. Wilson, G. M. Wolfe, C. T. Woods, and L. H. Zeng (2018), ATom: Merged Atmospheric Chemistry, Trace Gases, and Aerosols, ORNL DAAC, doi: <https://doi.org/10.3334/ORNLDAA/1581>.

Yang, S., B. X. Chang, M. J. Warner, T. S. Weber, A. M. Bourbonnais, A. E. Santoro, A. Kock, R. E. Sonnerup, J. L. Bullister, S. T. Wilson, and D. Bianchi (2020), Global reconstruction reduces the uncertainty of oceanic nitrous oxide emissions and reveals a vigorous seasonal cycle, *Proceedings of the National Academy of Sciences*, p. 201921914, doi: 10.1073/pnas.1921914117.